JOURNAL OF COMPUTATIONAL PHYSICS **144,** 550–602 (1998)
ARTICLE NO. CP985983

A Model for the Simulation of Turbulent Boundary Layers in an Incompressible Stratified Flow

Donald N. Slinn[1] and J. J. Riley

Department of Mechanical Engineering, University of Washington, Seattle, Washington 98195

Received July 21, 1997; revised February 12, 1998

A model with several original physical and numerical features has been developed for direct numerical and large eddy simulations of a turbulent boundary layer in a stratified fluid. The large scale flow for which the model was developed involves internal waves reflecting from a sloping boundary. In the model, the internal waves are generated by a new technique that forces monochromatic waves at specified wavelengths and frequencies. A new analytic solution has been obtained representative of the forcing conditions. In the model, time discretization is based upon the projection method incorporating a third-order Adams–Bashforth scheme with variable time steps, and spatial discretization employs fourth-order compact differencing techniques on a variable grid that increases resolution close to the boundary. The model is periodic in two dimensions and in the third dimension employs an open boundary and a solid sloping surface. The pressure field is determined using a fast direct solution method of fourth-order accuracy. The model includes flow analysis aids such as tracking Lagrangian particles and advected scalar quantities. Flow measurements are made of the integrated kinetic and potential energy balances, local dissipation rates, and the energy spectra. The utility of the model is examined in a number of test problems. It appears that the model is well suited for simulations of transitioning and turbulent boundary layers.

1. INTRODUCTION

A number of important fluid flows involve turbulent boundary layers. Such boundary layers are among the most difficult types of flows to compute because they contain a wide range of spatial and temporal scales. Spalart *et al.* (1991) were first to develop a Navier–Stokes solver for the direct numerical simulation (DNS) of a turbulent boundary layer. Their

[1] Mailing address: College of Oceanic and Atmospheric Sciences, Oregon State University, Oceanography Administration Building 104, Corvallis, OR 97331-5503.

0021-9991/98 $25.00

model employed a semi-infinite, doubly periodic domain utilizing spectral basis functions to examine the dynamics of a constant density fluid. Rai and Moin (1993) simulated a spatially evolving boundary layer over a flat plate using a finite difference scheme. In this paper we describe a model for the direct numerical simulation of transitioning and turbulent boundary layers in a stratified (i.e., variable density) incompressible fluid.

Our model was designed to study the problem of internal wave reflection from sloping boundaries. When an internal gravity wave reflects from a sloping boundary, the wave's energy density and amplitude may increase significantly, especially if the angle of propagation of the wave is close to the angle of the bottom slope. The reflection can result in wave breakdown into a turbulent layer near the boundary, a process thought to make a large contribution to vertical mixing in the ocean (Eriksen, 1998). To model this process, we have developed a new method for generating a monochromatic oncoming train of internal gravity waves of specified wavelength and frequency. Also, an analytic solution is developed for the wave forcing mechanism that predicts properties of the resulting forced wave. We present results from experiments of internal wave reflection from sloping boundaries in which flow near the the boundary transitions to turbulence.

Several recent advances in numerical techniques are incorporated into the model, which solves the three-dimensional Navier–Stokes equations for a stratified flow subject to the Boussinesq approximation. High resolution is achieved in the near-wall region by utilizing a variable or clustered grid in physical space, with an increasing density of computational points near the boundary. The variable grid is mapped onto a uniform grid in computational space by an analytic function. The spatial discretization in the model uses compact finite-differencing techniques (Lele, 1992), which have near-spectral accuracy in their ability to resolve a wide range of wavenumbers. This is especially important in accurately treating wave propagation. The time discretization scheme incorporates the pressure projection method (e.g., Karniadakis *et al*., 1991) with a third-order Adams–Bashforth time-stepping scheme that recalculates a stable time step during the time integration in order to achieve optimum use of computational resources. The model has periodic boundary conditions in two directions and employs an open boundary condition at the top boundary and a solid surface at the bottom boundary. A fast direct pressure solution method has been implemented, which takes advantage of the periodicity of the problem. The code has been optimized for vector and parallel processor computers and is used with grid resolutions of approximately 128^3 grid points.

The basic mathematical model and the model problem to be studied are described in Section 2, and the numerical methods are described in detail in Section 3. Section 4 presents simulation results from a number of test problems, and Section 5 contains the summary and conclusions.

2. INCOMPRESSIBLE STRATIFIED FLOW MODEL

Considering forced, dissipative, incompressible flow within the Boussinesq approximation (Phillips, 1977), the conservation equations for mass, momentum, and internal energy (or, salinity for a liquid) are, respectively,

$$\tilde{\nabla} \cdot \tilde{\mathbf{u}} = 0, \tag{2.1}$$

$$\frac{\partial \tilde{\mathbf{u}}}{\partial \tilde{t}} + \tilde{\mathbf{u}} \cdot \tilde{\nabla}\tilde{\mathbf{u}} = -\frac{\tilde{\nabla}\tilde{p}}{\rho_o} - \hat{k}\frac{g}{\rho_o}\tilde{\rho} + \nu\tilde{\nabla}^2\tilde{\mathbf{u}} + \tilde{\mathbf{F}}_{\mathbf{u}}, \tag{2.2}$$

$$\frac{\partial \tilde{\rho}}{\partial \tilde{t}} + \tilde{\mathbf{u}} \cdot \tilde{\nabla} \tilde{\rho} + \tilde{\omega} \frac{d\bar{\rho}}{d\tilde{z}} = \kappa \tilde{\nabla}^2 \tilde{\rho} + \tilde{F}_\rho. \tag{2.3}$$

Equations (2.1)–(2.3) are five equations for the five unknowns $\tilde{\mathbf{u}} = (\tilde{u}, \tilde{v}, \tilde{w})$, $\tilde{p}$, and $\tilde{\rho}$, where the $\tilde{}$ represents a dimensional quantity. Here $\tilde{\mathbf{u}}$ is the fluid velocity, g is the gravitational acceleration, $\tilde{p}$ is the perturbation pressure field, $\tilde{\mathbf{x}} = (\tilde{x}, \tilde{y}, \tilde{z})$ is the Cartesian coordinate system with unit vector $\hat{\mathbf{i}} = (\hat{i}, \hat{j}, \hat{k})$ (where $\tilde{z}$ is in the vertical direction, $\tilde{\rho}$ is the fluctuating density field, ρ_o is the constant background density, and $\frac{d\bar{\rho}}{d\tilde{z}}$ is the background density stratification (assumed here to be constant), which will be negative in all cases considered in this work (i.e., density increasing with depth in the ocean or decreasing with height in the atmosphere.) A body force $\tilde{\mathbf{F}}_\mathbf{u} = (\tilde{F}_u, \tilde{F}_v, \tilde{F}_w)$ is applied to the momentum equation, and the density field is forced with $\tilde{F}_\rho$. The parameters ν and κ are coefficients of diffusion of momentum and density.

Density fluctuations and stratification are considered small compared with ρ_o in the Boussinesq approximation. The total density and pressure fields may be written

$$\tilde{\rho}_t = \rho_o + \frac{d\bar{\rho}}{d\tilde{z}} \tilde{z} + \tilde{\rho}, \tag{2.4}$$

$$\tilde{p}_t = p_o + \tilde{p}. \tag{2.5}$$

Here, p_o is a reference state in hydrostatic balance with the background density field in the Boussinesq approximation, e.g.,

$$\frac{dp_o}{d\tilde{z}} = -\rho_o \, g \, \tilde{z}. \tag{2.6}$$

In the Boussinesq approximation $|-\rho_o \, g \, \tilde{z}| \gg |\frac{d\bar{\rho}}{d\tilde{z}} \tilde{z} \, g \, \tilde{z}|$, so hydrostatic balance is only between pressure and the background density field to the order of the approximation. The hydrostatic balance has already been removed from (2.2), which is written in terms of pressure and density fluctuations.

The governing equations may be nondimensionalized as

$$\mathbf{u} = \frac{\tilde{\mathbf{u}}}{U}, \qquad \mathbf{x} = \frac{\tilde{\mathbf{x}}}{L}, \qquad t = \frac{\tilde{t}}{L/U}, \qquad p = \frac{\tilde{p}}{\rho_o U^2}, \qquad \rho = \frac{\tilde{\rho}}{L|d\bar{\rho}/d\tilde{z}|},$$

$$\mathbf{F}_\mathbf{u} = \frac{\tilde{\mathbf{F}}_\mathbf{u}}{U^2/L}, \qquad F_\rho = \frac{\tilde{F}_\rho}{U|d\bar{\rho}/d\tilde{z}|}. \tag{2.7a–2.7g}$$

Here U is the characteristic velocity, L is a characteristic (vertical) length scale, pressure is nondimensionalized with the dynamic pressure, and density is nondimensionalized using the background density gradient. With (2.7), the momentum equation, (2.2), becomes

$$\frac{\partial \mathbf{u}}{\partial t} + \mathbf{u} \cdot \nabla \mathbf{u} = -\nabla p - \hat{k} \, Ri \, \rho + \frac{1}{Re} \nabla^2 \mathbf{u} + \mathbf{F}_\mathbf{u}. \tag{2.8}$$

The nondimensional parameters (the Froude, Richardson, Reynolds, Prandtl, and Peclet numbers) are

$$Fr = \frac{U}{NL}, \qquad Ri = \left(\frac{NL}{U}\right)^2, \qquad Re = \frac{UL}{\nu}, \qquad Pr = \frac{\nu}{\kappa}, \qquad Pe = Re \, Pr, \tag{2.9a–2.9e}$$

where the buoyancy frequency, N, is defined by

$$N^2 = \left(\frac{-g}{\rho_o} \frac{d\bar{\rho}}{d\tilde{z}} \right). \tag{2.10}$$

Using (2.7) in (2.1) gives

$$\nabla \cdot \mathbf{u} = 0. \tag{2.11}$$

The governing equation, (2.3), for the density field becomes

$$\frac{\partial \rho}{\partial t} + \mathbf{u} \cdot \nabla \rho - w = \frac{1}{Pe} \nabla^2 \rho + F_\rho. \tag{2.12}$$

2.1. *Problem Geometry*

The model problem is taken to be periodic in the x- and y-directions and bounded by a plane wall at the bottom boundary. To accommodate a sloping ocean floor, it is advantageous to rotate the coordinate system about the y axis by the angle of the slope, α, so that the x axis is directed upslope, y is across-slope, and z is perpendicular to the slope (Fig. 1). This rotation complicates some other aspects of the problem. For example, the x component of the momentum equation has a component of the gravity force, and the density equation has the velocity component u (in addition to w) multiplying the mean density gradient. The background density and pressure fields are not periodic at the lateral boundaries in x. Because the background fields have been subtracted from the governing equations, however, if the remaining perturbation density and pressure fields are initially periodic in the x direction, they will remain so.

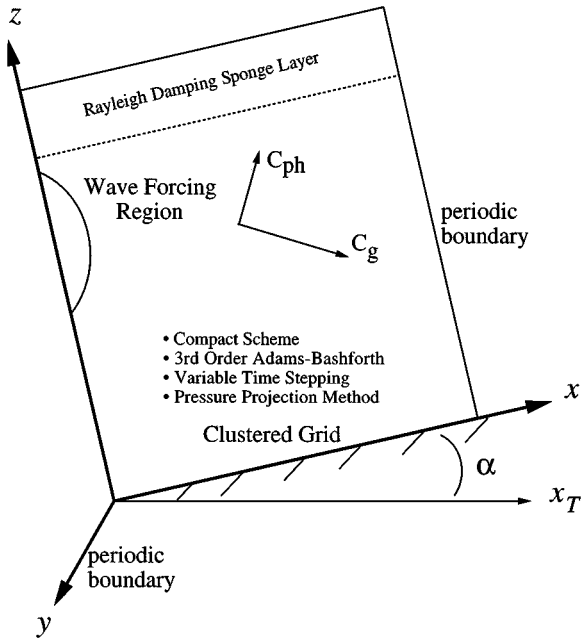

FIG. 1. The computational domain and suggestions of some of the key numerical methods utilized in the model.

Hereinafter, for convenience, x_T and z_T will be used to designate the true horizontal and vertical directions, perpendicular and parallel to gravity. Thus, the governing equations, (2.8), (2.11), and (2.12), for a coordinate system rotated through angle α are

$$\frac{\partial u}{\partial x} + \frac{\partial v}{\partial y} + \frac{\partial w}{\partial z} = 0, \tag{2.13}$$

$$\frac{\partial u}{\partial t} + u\frac{\partial u}{\partial x} + v\frac{\partial u}{\partial y} + w\frac{\partial u}{\partial z} + Ri\,\rho \sin\alpha = -\frac{\partial p}{\partial x} + \frac{1}{Re}\left(\frac{\partial^2 u}{\partial x^2} + \frac{\partial^2 u}{\partial y^2} + \frac{\partial^2 u}{\partial z^2}\right) + F_u, \tag{2.14}$$

$$\frac{\partial v}{\partial t} + u\frac{\partial v}{\partial x} + v\frac{\partial v}{\partial y} + w\frac{\partial v}{\partial z} = -\frac{\partial p}{\partial y} + \frac{1}{Re}\left(\frac{\partial^2 v}{\partial x^2} + \frac{\partial^2 v}{\partial y^2} + \frac{\partial^2 v}{\partial z^2}\right) + F_v, \tag{2.15}$$

$$\frac{\partial w}{\partial t} + u\frac{\partial w}{\partial x} + v\frac{\partial w}{\partial y} + w\frac{\partial w}{\partial z} + Ri\,\rho \cos\alpha = -\frac{\partial p}{\partial z} + \frac{1}{Re}\left(\frac{\partial^2 w}{\partial x^2} + \frac{\partial^2 w}{\partial y^2} + \frac{\partial^2 w}{\partial z^2}\right) + F_w, \tag{2.16}$$

$$\frac{\partial \rho}{\partial t} + u\frac{\partial \rho}{\partial x} + v\frac{\partial \rho}{\partial y} + w\frac{\partial \rho}{\partial z} - w\cos\alpha - u\sin\alpha = \frac{1}{Pr\,Re}\left(\frac{\partial^2 \rho}{\partial x^2} + \frac{\partial^2 \rho}{\partial y^2} + \frac{\partial^2 \rho}{\partial z^2}\right) + F_\rho. \tag{2.17}$$

2.2. *Initial Conditions*

The reflection of internal waves from the ocean floor can be modeled numerically either by solving an initial value problem of a downward propagating wave packet (examined in this section), or by creating continuous wave source in the computational domain (Subsection 2.3). The initial conditions consist of combinations of three distinct parts: a wave packet, laminar boundary currents, and a background flow consisting of white noise or low level turbulence. Gravity waves may be initialized by specifying the wave as a perturbed density field, together with the instantaneous velocities associated with the wave.

The initial value problem in which the flow field is set to represent a wave packet propagating downward at angle θ with respect to the horizontal, with group velocity $\vec{C}_g$ and wavenumber $\mathbf{k} = (k, l, m)$, is presented here following Winters (1989). The analytic expression for a wave packet localized in z is determined by seeking a sinusoidal solution to the linearized non-diffusive governing equations.

$$u(x, y, z, 0) = -\frac{Am}{k}F(z)\cos(kx + mz) - \frac{A}{k}F'(z)\sin(kx + mz), \tag{2.18}$$

$$v(x, y, z, 0) = 0 \tag{2.19}$$

$$w(x, y, z, 0) = AF(z)\cos(kx + mz), \tag{2.20}$$

$$\rho(x, y, z, 0) = \frac{-A\cos\alpha F(z)}{\omega}\sin(kx + mz) + \frac{Am\sin\alpha F(z)}{\omega k}\sin(kx + mz) - \frac{A\sin\alpha F'(z)}{\omega k}\cos(kx + mz). \tag{2.21}$$

The function $F(z)$ with derivative $F'(z)$ has been suggested by Winters (1989) in order to localize the wave packet in the computational domain

$$F(z) = \exp[-b(z - z_0)^2], \qquad 0 \le z \le L_z, \tag{2.22}$$

where the (x, y, z) dimensions of the domain are (L_x, L_y, L_z). The term $F'(z)$ ensures the non-divergence of the wave packet. To minimize dispersive effects the vertical extent of the wave packet should be somewhat longer than the vertical wavelength $\lambda_z = 2\pi/m$ of the gravity waves. Typical parameters used in the model initialization are

$$z_0 = \frac{L_z}{2}, \qquad A = \frac{\tilde{w}}{U} = 0.015, \qquad b = \frac{30}{L_z^2}, \qquad k = \frac{2\pi}{\lambda_x} = \frac{2\pi}{3},$$

$$l = 0, \qquad m = \frac{2\pi}{\lambda_z} = 2\pi. \tag{2.23a–2.23f}$$

The dispersion relation of the wave packet is given by

$$\omega^2 = \frac{Ri(k\cos\alpha - m\sin\alpha)^2}{k^2 + m^2}. \tag{2.24}$$

The phase and group velocities are perpendicular (Phillips, 1977), and their magnitudes are related by $|\vec{C}_g| = |\vec{C}_{ph}| m/k$ where

$$\vec{C}_{ph} = \frac{\sqrt{Ri}(k\cos\alpha - m\sin\alpha)}{(k^2+m^2)^{3/2}}(k\hat{i} + m\hat{k}), \tag{2.25}$$

$$\vec{C}_g = \frac{\sqrt{Ri}(m\cos\alpha + k\sin\alpha)}{(k^2+m^2)^{3/2}}(m\hat{i} - k\hat{k}). \tag{2.26}$$

The wave and buoyancy periods are, respectively,

$$T_w = \frac{2\pi}{\sqrt{Ri}\sin\theta}, \tag{2.27}$$

$$T_B = \frac{2\pi}{\sqrt{Ri}}. \tag{2.28}$$

A wave with group velocity propagating downward and in the positive x and y directions at angle θ to the horizontal has wave numbers defined from $\theta = \tan^{-1}(m/k) - \alpha$. In the flat bottom case ($\alpha = 0$) positive values for k and m yield a wave packet that propagates in the positive x and negative z directions. This is not generally the case for arbitrary angle α. For instance, when $k\cos\alpha - m\ \sin\alpha < 0$, positive wavenumbers can lead to a wave packet propagating in the negative x direction.

Constant density contours of a large amplitude initial wave packet with peak amplitude $\frac{3A_0}{4}$, where A_0 is the amplitude of an overturning wave, are shown in Fig. 2. The direction of propagation of the phase and group velocities are indicated on the figure. Note that even though the waves in this packet are of somewhat large amplitude they are not near the point of incipient breaking (amplitude A_0, where $\partial\rho_t/\partial z_T = 0$ at the steepest point).

2.3. *Mechanical Wave Forcing*

A second method to generate incoming waves is to force them continuously from inside the computational domain during the simulation. This is accomplished by utilizing the forcing terms on the right hand sides of the governing equations. A simplified variation of this method was introduced by Fovell *et al.* (1992). In our model both the velocity and density fields are locally forced in a manner that generates a monochromatic wave train with specified frequency and wavenumber vector incident upon the sloping terrain. This method

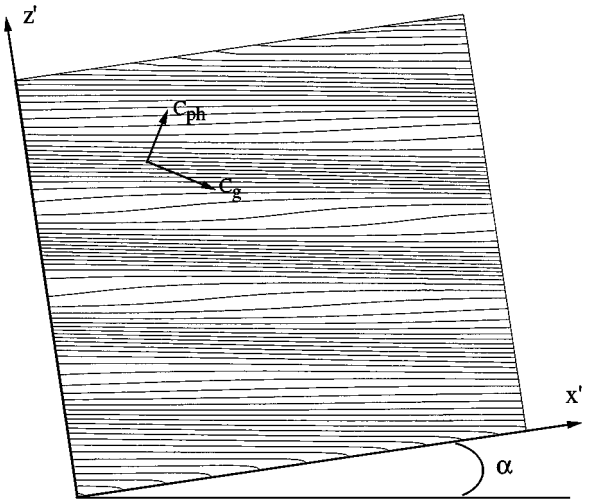

FIG. 2. For the initial value problem, density contours are shown of the initial wave packet with amplitude $0.75A_0$, 3/4 the amplitude of an overturning wave.

offers several advantages over the wave packet approach, such as allowing a longer time for the waves to break down and providing close comparison with laboratory experiments. Additional flexibility with the wave source may be gained by using a time dependent forcing amplitude $A(t)$ without modification.

The forcing functions in the rotated coordinate system are specified using similar relations to those used for the wave packet, e.g.,

$$F_u = -\frac{Am}{k}F(z)\cos(kx + mz - \omega t) - \frac{A}{k}F'(z)\sin(kx + mz - \omega t), \tag{2.29}$$

$$F_v = 0 \tag{2.30}$$

$$F_w = AF(z)\cos(kx + mz - \omega t), \tag{2.31}$$

$$F_\rho = \frac{-A\cos\alpha F(z)}{\omega}\sin(kx + mz - \omega t) + \frac{Am\sin\alpha F(z)}{\omega k}\sin(kx + mz - \omega t) - \frac{A\sin\alpha F'(z)}{\omega k}\cos(kx + mz - \omega t), \tag{2.32}$$

where the localization function $F(z)$ is given by (2.22), but is more strongly localized (larger b) and centered at $z_0 = 2L_z/3$. Experience indicates that choosing the vertical extent of $F(z)$ equal to the vertical wavelength of the desired monochromatic wave train yields satisfactory results (Subsection 2.3.1).

The internal wave train is started from rest, and after a short startup period, a quasi-steady flow develops in which a beam of sinusoidal internal waves propagate toward the bottom boundary. Figure 3 shows isopycnals of the waves emerging from the region of wave forcing, waves that have grown in amplitude due to interactions with the sloping bottom boundary, and wave breakdown beginning to occur.

The forcing functions F_u and F_w may be written in terms analogous to a stream function, e.g.,

$$F_u = -\frac{\partial\Psi}{\partial z}, \qquad F_w = \frac{\partial\Psi}{\partial x}, \tag{2.33a–2.33b}$$

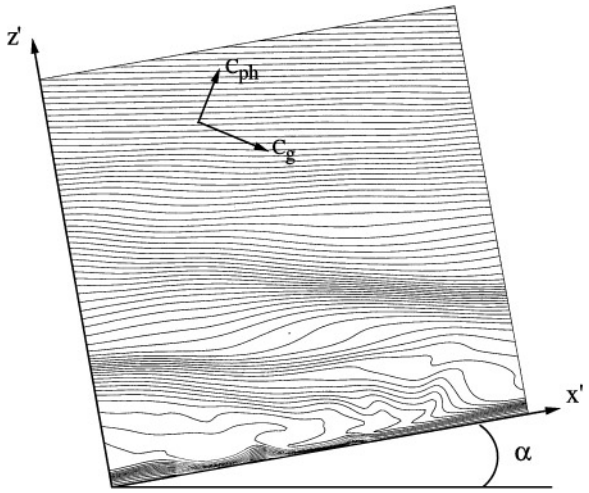

FIG. 3. Steady wave forcing showing constant density surfaces of an internal wave propagating downward toward the bottom boundary from the forcing region.

which will be mathematically convenient in the next section. The stream function Ψ is

$$\Psi = \frac{A(t)F(z)}{k}\sin(kx + mz - \omega t). \tag{2.34}$$

2.3.1. *Analytic Solution.* An analytic solution can be obtained for the wave train that propagates from the forcing region, obtained by writing the linearized equations of motion with forcing added and searching for solutions whose time dependence is wavelike. We analyze the case with $\alpha = 0$ for simplicity and begin with the linearized system

$$\frac{\partial u}{\partial t} = -\frac{\partial p}{\partial x} - \frac{\partial \Psi}{\partial z}, \tag{2.35}$$

$$\frac{\partial w}{\partial t} = -Ri\,\rho - \frac{\partial p}{\partial z} + \frac{\partial \Psi}{\partial x}. \tag{2.36}$$

$$\frac{\partial \rho}{\partial t} = w + F_\rho. \tag{2.37}$$

Pressure may be eliminated from the system using a stream function, with $u = \frac{\partial \psi}{\partial z}$ and $w = -\frac{\partial \psi}{\partial x}$. Taking the curl of the linearized momentum equations and adding them yields

$$\frac{\partial}{\partial t}\nabla^2\psi - Ri\frac{\partial \rho}{\partial x} = -\nabla^2\Psi. \tag{2.38}$$

Density may be eliminated from (2.38) using (2.37) which gives

$$\frac{\partial^2}{\partial t^2}\nabla^2\psi + Ri\frac{\partial^2 \psi}{\partial x^2} = -\frac{\partial}{\partial t}\nabla^2\Psi + Ri\frac{\partial F_\rho}{\partial x}. \tag{2.39}$$

Here Ψ and F_ρ are specified by (2.34) and (2.33), with $A(t) = A$, a constant; therefore, the right hand side of (2.39) is

$$-\frac{A\omega}{k}[2(k^2+m^2)F(z) - F''(z)\cos\phi + 2mF'(z)\sin\phi], \tag{2.40}$$

where $\phi = (kx + mz - wt)$.

A solution to the system may be found of the form

$$\psi = A_f(z)\cos\phi + B_f(z)\sin\phi, \tag{2.41}$$

for which the entire time dependence of the solution is contained in the wave forms of $\sin\phi$ and $\cos\phi$. Substituting ψ into (2.40) and equating the sine and cosine parts leads to the following third-order equations for $A_f(z)$ and $B_f(z)$

$$B_f'''(z) + 4m^2 B_f'(z) = \frac{4Am}{\omega k}(k^2+m^2)F(z) = C_1 F(z) \tag{2.42}$$

$$A_f'''(z) + 4m^2 A_f'(z) = -\frac{A}{\omega k}F'''(z) + \frac{2A(k^2-m^2)}{\omega k}F'(z) = C_2 F'''(z) + C_3 F'(z). \tag{2.43}$$

For certain specified forms of $F(z)$ on the interval $0 < z < \pi$, such as $F(z) = \sin^2(z)$, analytic expressions for $A_f(z)$ and $B_f(z)$ can be found. For example, for $F(z) = \sin^2(z)$, the analytic solution is given in Appendix A. For the form of $F(z)$ used above, however, a numerical solution of the third-order ordinary differential equations (2.42) and (2.43) is obtained by inverting a pentadiagonal matrix representing a finite difference discretization for the derivatives of $A_f(z)$ and $B_f(z)$. The relative magnitudes of C_1, C_2, and C_3 to $4m^2$ are the important parameters that determine the shape of the solutions for $A_f(z)$ and $B_f(z)$.

The numerical solution is approximated at the interior nodes with fourth and second order accurate stencils for the derivatives, e.g.,

$$B_f'(z) = \frac{-B_{i+2} + 8B_{i+1} - 8B_{i-1} + B_{i-2}}{12\Delta z}, \tag{2.44}$$

$$B_f'''(z) = \frac{B_{i+2} - 2B_{i+1} + 2B_{i-1} - B_{i-2}}{2\Delta z^3}. \tag{2.45}$$

Three boundary conditions on $B_f(z)$ are used, assuming the z-component of the wave group velocity is negative: as $z \to \infty$, $B_f = 0$ and $B_f' = 0$, and as $z \to -\infty$, $B_f' = 0$. The same boundary conditions are used for $A_f(z)$. An alternate solution method has also been used, yielding equivalent results, by solving Eq. (2.43) for $B_f'(z)$, using the method of variation of parameters, and numerically integrating both the right hand side of the equation and B_f' to find B_f.

Figure 4 shows solutions for $A_f(z)$ and $B_f(z)$ for the shape function of the forcing region, $F(z)$, indicated. Here m (the vertical wavenumber) is chosen so that $\lambda_z = 2\pi/m$ is smaller ($\lambda_z \approx L_F/1.6$) than the characteristic length scale of $F(z)$, defined by L_F, which is the width of $F(z)$ at $F(z) = F_{max}/10$. The solutions indicate that the signal coming out of the forcing region, $B_f \sin\phi$, is steady and smooth and confined within the carrier wave envelope B_f shown. The envelope's smoothness is a function of the ratio of $\frac{2\pi}{m}/L_F$. When this ratio is

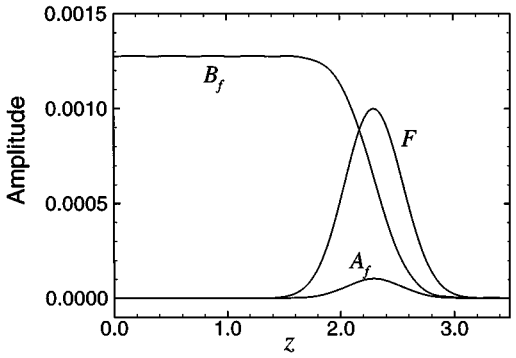

FIG. 4. Signal shape function for $A_f(z)$ and $B_f(z)$ for a broad forcing region ($L_F = 1.6\lambda_z$) of shape $F(z)$ and wavelength $\lambda_z = 0.7$.

greater than one, such that the forcing region is wider than a vertical wavelength of the forced wave, then the signal that emerges has the desirable features of being uniform in shape and time. When the forcing region is narrower than a wavelength of the emitted signal, then the output is modulated by an irregular, non-constant envelope. In Fig. 4 the emitted signal propagates from right to left (downward). $B_f(z)$ represents the shape of the internal wave train emerging from the forcing region having the $\sin\phi$ dependence. $A_f(z)$ represents a local disturbance with $\cos\phi$ dependence within the forcing region, which satisfies the non-divergence criteria required by incompressible flow. $A_f(z)$ vanishes outside of the forcing region due to the symmetry of $F(z)$ when the forcing region is sufficiently broad.

Figures 5 and 6 show solutions for relatively broad and narrow forcing regions defined by ratios of $\frac{2\pi}{m}/L_f$ of 1.05 and 0.73. The envelope and signal wavelength are shown here in comparison with the forcing region width. Figure 5 shows a satisfactorily smooth signal coming from a broad forcing region, and Fig. 6 shows the modulated signal and envelope coming from a narrower forcing region. These analytic results have been tested by numerical simulations that verify the influence and importance of the width of the wave forcing region compared to the vertical wavelength. The main result is that, for satisfactory resolution (so that an unmodulated wave is produced), the forcing region should be wider than a vertical wavelength of the emitted wave.

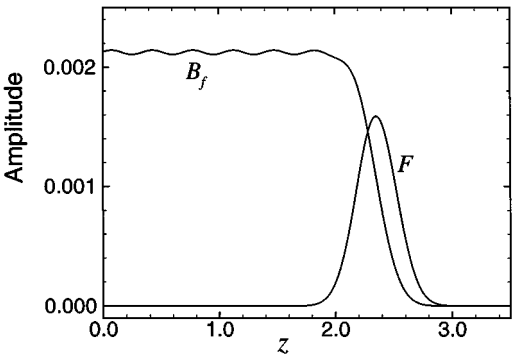

FIG. 5. A marginally broad forcing region, approximately the same width as the vertical wavelength of the emitted wave ($L_F = 1.05\lambda_z$), has fairly smooth properties for the shape function $B_f(z)$. Also shown is the forcing region, $F(z)$, with height normalized to be of the same scale as B_f.

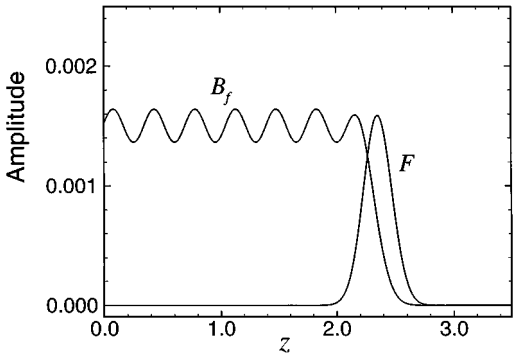

FIG. 6. A narrow forcing region, smaller in width than the vertical wavelength of the emitted sine wave ($L_F = 0.73\lambda_z$), leads to oscillations in the shape function $B_f(z)$. Also shown is the forcing region, $F(z)$, with height normalized to be of the same scale as B_f.

2.4. *White Noise and Turbulence*

The wave packet and wave train described above are two-dimensional (i.e., the oncoming wave approaches the wall in the plane of the slope). In this case additional flow features are required to break the symmetry of the problem and allow the reflected waves to break down three-dimensionally. To accomplish this a small amount of white noise is added to the background flow. Experience has shown that a background noise level that contains roughly one percent of the local energy density of the oncoming wave train is sufficient to allow wave instabilities to develop quickly and cause the waves to break into turbulence.

This white noise is generated by taking the incompressible projection of a pseudo-random velocity field localized near the wall. The density field is also initialized with random fluctuations added to the background profile. These perturbation velocity and density fields are filtered to remove energy at high wave numbers and then set in motion for about one buoyancy period. This allows the noise field to begin to develop into low level turbulence containing some coherence. After a short developmental period a wave packet is superimposed on the background noise field, or the wave forcing is initiated, and the waves begin to propagate toward the wall.

2.5. *Boundary Conditions*

A periodic domain in x and y, consistent with the periodicity of the oncoming wave, is chosen to simplify boundary conditions at the lateral boundaries. The lateral (periodic) boundary conditions are

$$(u, v, w, p, \rho)(x, y, z, t) = (u, v, w, p, \rho)(x + L_x, y, z, t), \quad (2.46a)\text{–}(2.46e)$$

$$(u, v, w, p, \rho)(x, y, z, t) = (u, v, w, p, \rho)(x, y + L_y, z, t). \quad (2.47a)\text{–}(2.47e)$$

No slip boundary conditions are specified at the bottom boundary ($z = 0$) with

$$u(x, y, 0, t) = 0, \qquad v(x, y, 0, t) = 0, \qquad w(x, y, 0, t) = 0. \quad (2.48a)\text{–}(2.48c)$$

The bottom boundary condition for density is a no-flux condition, equivalent, in a temperature stratified fluid, to an adiabatic boundary condition. In a salt stratified fluid the no-flux

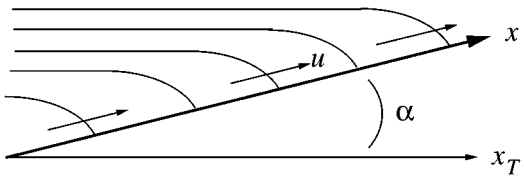

FIG. 7. Isopycnals near a sloping boundary with an adiabatic boundary condition showing secondary currents generated for a constant interior stratification.

boundary condition means that there are no sources or sinks of salt at the wall, so that the salt in the interior flow is conserved. A no-flux wall may be simulated with the condition

$$\left.\frac{\partial \rho_t}{\partial z}\right|_b = 0, \tag{2.49}$$

where, with the nondimensionalization specified above, $\rho_t = \rho_o - z\cos\alpha - x\sin\alpha + \rho$ is the total density field. In practice (2.49) is written in terms of the normal derivative of the perturbation density

$$\left.\frac{\partial \rho}{\partial z}\right|_b = \cos\alpha, \tag{2.50}$$

a constant.

Phillips (1970) and Wunsch (1970) have shown that a no-flux boundary condition can give rise to a steady circulation in a density stratified fluid in which mass diffusion is balanced by upslope convection near the boundary. Figure 7 shows the total density contours in the near-wall region for the steady flow, and Fig. 8 illustrates the velocity profile. For typical experiments conducted in this study, with intermediate bottom slopes (e.g., $5^\circ < \alpha < 30^\circ$) and moderate Reynolds numbers ($Re \simeq 1000$), the steady profiles develop on time scales fast compared with wave propagation time scales. Consequently, the flow is initialized to include the fully developed steady laminar profiles, as given by

$$\rho(z) = \frac{-\cos\alpha e^{-\gamma z}\cos\gamma z}{\gamma}, \tag{2.51}$$

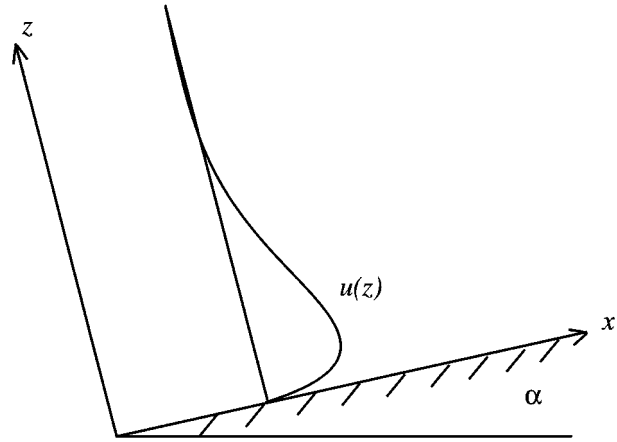

FIG. 8. Alongslope velocity profiles to maintain steady-state buoyancy boundary currents.

$$u(z) = \frac{2\gamma \cot\alpha e^{-\gamma z} \sin\gamma z}{Pr\, Re}, \tag{2.52}$$

$$w(z) = v(z) = 0, \tag{2.53}$$

where $\gamma = (Ri\, Pr\, Re^2 \sin^2 \alpha/4)^{1/4}$.

The upper boundary condition is chosen to be a radiative boundary condition, allowing waves to freely propagate out of the computational domain. Its presentation is deferred to Subsection 3.4 (dealing with numerical boundary conditions). This upper boundary condition is implemented using Rayleigh damping in the top region of the domain.

2.6. *Model Summary*

Experience with numerical simulation has shown the advisability of solving implicitly for the pressure field, to allow it to adjust instantaneously to the velocity field in such a manner as to ensure incompressible flow. This approximation of infinitely fast pressure waves is warranted for low Mach number (incompressible) flows, since pressure waves propagate much faster (acoustic speeds) than other adjustments (gravity waves, turbulence) in the flow. The governing equation for the pressure is a Poisson equation. It may be derived by taking the divergence of the momentum equation (2.8), summing the components, and using the continuity equation to simplify. The pressure projection method is used to treat the pressure field and is detailed below in Subsection 3.3.

For the three-dimensional model, the system to be solved numerically comprises Eqs. (2.13)–(2.17) with the appropriate pressure equation to be presented below, together with an appropriate set of boundary conditions from (2.46)–(2.50), upper boundary conditions to be presented later, and initial conditions from (2.18)–(2.21) and (2.51)–(2.53), or a mechanical wave source as given by (2.29)–(2.32).

3. NUMERICAL METHODS

Two numerical codes have been developed in this study, for two-dimensional (2-D) and three-dimensional (3-D) flows. Numerical methods used in these codes are outlined below, primarily in the context of the three-dimensional model. Except where noted, the two-dimensional model uses the same algorithms. The standard resolution for the two-dimensional model is 201×401 grid points; the three-dimensional model uses grid resolutions of up to $129 \times 129 \times 130$ grid points.

The model uses a single spatial grid at which all of the variables (u, v, w, p, and ρ) and their spatial derivatives are determined as recommended by Shih *et al*. (1989) using the fourth-order compact scheme. The nonlinear terms are calculated in advective form, e.g., $u\frac{\partial u}{\partial x}$. The model conserves mass, momentum, and energy to a high degree of accuracy. The time marching technique employs an explicit fractional step method in which the pressure terms are treated separately. Significant model features include a variable time stepping procedure, a variable grid with increased resolution in the boundary layer, an open upper boundary condition, a direct pressure solver, and a number of flow measurement techniques.

3.1. *Spatial Discretization*

Velocity and pressure derivatives are calculated using Hermitian compact (or Padé) techniques, following the work of Hirsh (1975), Adam (1977), and Lele (1992). These methods

offer improved resolution over traditional finite-difference schemes, and spectral-like behavior in their ability to represent a wide range of wavenumbers accurately. In addition, the compact scheme has minimal phase errors, an important property for wave propagation problems, and may be used in other applications such as spectral-like filtering (Lele, 1992).

The Padé representation of the first derivative results in a tridiagonal system of the form

$$\frac{1}{3}u_{x(i+1)} + \frac{4}{3}u_{xi} + \frac{1}{3}u_{x(i-1)} = \frac{1}{h}(u_{i+1} - u_{i-1}), \tag{3.1}$$

where h is the distance between grid points, and the velocity derivatives are written $\partial u/\partial x|_i \equiv u_{xi}$. The scheme is called "compact" because it involves relations between grid points on a smaller stencil than the standard finite difference formula. The truncation error for the compact scheme, $-h^4 \frac{\partial^5 u}{\partial x^5}|_i/180$, is one sixth the truncation error of the standard Taylor series scheme.

Formal fourth-order accuracy is maintained throughout the numerical model. Second-derivatives are calculated using the compact representation

$$\frac{1}{12}u_{xx(i+1)} + \frac{5}{6}u_{xxi} + \frac{1}{12}u_{xx(i-1)} = \frac{1}{h^2}(u_{i+1} - 2u_i + u_{i-1}), \tag{3.2}$$

where $\partial^2 u/\partial x^2|_i \equiv u_{xxi}$. The boundary nodes for first- and second-derivatives require special treatment and will be described below.

It is well known that boundary schemes may be one order less accurate than an interior domain scheme without degrading the overall accuracy of the interior difference scheme (e.g., Kreiss, 1972). Third-order accurate boundary schemes for Dirichlet boundary conditions (u is specified at the boundary) are suggested by Adam (1977),

$$2u_{x1} + 4u_{x2} = \frac{1}{h}(-5u_1 + 4u_2 + u_3), \tag{3.3}$$

$$4u_{x2} + 2u_{x3} = \frac{1}{h}(-u_1 - 4u_2 + 5u_3), \tag{3.4}$$

$$2u_{x(m-2)} + 4u_{x(m-1)} = \frac{1}{h}(-5u_{m-2} + 4u_{m-1} + u_m), \tag{3.5}$$

$$4u_{x(m-1)} + 2u_{xm} = \frac{1}{h}(-u_{m-2} - 4u_{m-1} + 5u_m), \tag{3.6}$$

where $i = m$ represents the last (maximum) grid point. The resulting tridiagonal matrix is computationally inexpensive to solve. When von Neumann boundary conditions are specified (the normal derivative $\partial u/\partial n$ is given on the boundary) the tridiagonal matrix is simplified, with all off diagonal elements equated to zero at the boundary by setting $u_{x1} = \partial u/\partial n$.

For the second derivative Lele (1992) suggests a third-order boundary condition compatible with the compact scheme for Dirichlet boundary conditions,

$$u_{xx1} + 11u_{xx2} = \frac{1}{h^2}[13u_1 - 27u_2 + 15u_3 - u_4]. \tag{3.7}$$

We have derived a third-order accurate von Neumann boundary condition for use with the

compact second derivative

$$29u_{xx1} + 85u_{xx2} = -\frac{78}{h}u_{x1} + \frac{1}{h^2}[-81u_2 + 84u_3 - 3u_4]. \tag{3.8}$$

The case of periodic boundary conditions is the simplest to implement numerically. The formulation maintains fourth-order spatial accuracy throughout. The resulting tri-diagonal matrix is not simply banded but includes two extra off-diagonal coefficients, one each in the upper-right and lower-left corners of the left-hand-side coefficient array. These additional coefficients do not present additional difficulties to inverting the matrix. Standard modifications for the Thomas (1949) tri-diagonal inversion algorithm are commonly available for the periodic case. The periodic boundaries are implemented in the model using a redundant grid point, e.g., $u_1 = u_m$.

3.2. *Spatial Filtering*

Spatial filtering is included as a feature of the model for two potential uses. First, the filter acts to partially de-alias the calculation, i.e., remove spurious accumulations of energy from the smallest scales of motion (Canuto *et al*., 1988, p. 118). When the filter is limited to this use the calculations can be considered as direct numerical simulations (DNS) of the flows. The second use of the filter, employed occasionally here, is as a simple subgrid-scale model. When used as a subgrid-scale model the filter is similar in principle to a hyperviscosity, (e.g., $\gamma\nabla^4\mathbf{u}$) that increases dissipation at smaller scales (higher wavenumbers). Hyperviscosity techniques are frequently used in simulations of geophysical flows (e.g., Winters, 1989; Lesieur, 1987). When the filter is used in this fashion the calculations are large-eddy simulations (LES).

In the gravity-wave reflection flow being studied, the main interactions that occur are at large scales and can be resolved. Both DNS and LES are used to investigate the flows over a large range of Reynolds numbers. For the cases with higher Reynolds number, using the large-eddy simulations, attention is focused on the large scales of motions and on the manner in which energy is transferred to the intermediate-scale motions; phenomena at the smaller, dissipative scales are parameterized. For these cases the model damps out interactions that occur on scales too small to be resolved on the numerical mesh. Two types of filtering techniques, the explicit and compact methods, are described below.

To enhance the performance of the finite difference method, a small amount of fourth-order spatial smoothing may be added to the right-hand sides of (2.13)–(2.17) to decrease aliasing errors without decreasing the formal accuracy of the scheme. Aliasing errors appear in finite-difference schemes mainly as the buildup of spurious amplitudes at the wavelengths corresponding to the smaller resolvable grid scales. In nonlinear equations, aliasing errors are related to the cascade of energy towards unresolvable scales, finer than the computational mesh. A one-dimensional fourth-order filter is of the form

$$\breve{u}_i = u_i - \gamma_4(u_{i+2} - 4u_{i+1} + 6u_i - 4u_{i-1} + u_{i-2}), \tag{3.9}$$

where $\breve{u}_i$ represents a filtered value of u_i, and γ_4 represents the strength of the filter. The filter is applied after the first half of the fractional time step (details below). The maximum stable value of γ_4 is $1/16$. For the boundary nodes, a boundary condition is known (e.g., no-slip) and no filter is used.

The filter in (3.9) is a second-order finite difference representation of the term $\gamma_4(\Delta x)^4(\partial^4 u/\partial x^4)$, which has a dissipative effect on u and smoothes the solution. The leading order truncation-error term resulting from taking derivatives with the compact scheme is of the form $O(\Delta x)^4(\partial^5 u/\partial x^5)$, which has dispersive effects on the solution. The fourth-order filter preserves the global fourth-order truncation error of the compact scheme. The addition of artificial diffusion by filtering helps the system maintain a smooth solution and does not degrade the overall fourth-order accuracy of the difference equations. Thus, filtering may alternatively be thought of simply as a desirable modification of the truncation errors. It is more common, however, to consider the addition of spatial filtering to the true viscous diffusion terms to be like a hyperviscosity, which is scale dependent, more strongly damping the small scale fluctuations.

It is advantageous to use the properties of the compact scheme to improve accuracy and scale selectivity of the spatial filter. Lele (1992) presents families of fourth- and sixth-order filters. He demonstrates compact filtering to be superior to explicit filtering for damping the shortest waves. In many formulations fourth-order compact filters confine their effects to higher wavenumbers than do sixth-order explicit filters. Explicit and compact filters of various order are compared in Fig. 9.

In the numerical model a fourth-order compact filter is used. The scheme requires solution of another tridiagonal matrix. Lele's Eq. (C.2.1),

$$\alpha_1 \breve{u}_{i-1} + \breve{u}_i + \alpha_1 \breve{u}_{i+1} = a_1 u_i + \frac{b_1}{2}(u_{i+1} + u_{i-1}) + \frac{c_1}{2}(u_{i+2} + u_{i-2}) + \frac{d_1}{2}(u_{i+3} + u_{i-3}), \tag{3.10}$$

represents the filtering process. The filter is represented by the transfer function, $T_c(\omega_c)$, satisfying $\breve{u}_j = T_c(\omega_c) u_j$, with Fourier component wave solutions

$$u_j = \hat{u}\, e^{i\omega_c j}, \qquad \omega_c = k\Delta x. \tag{3.11a)–(3.11b}$$

The transfer function (as shown in Fig. 9) for (3.10) is

$$T_c(\omega_c) = \frac{a_1 + b_1 \cos(\omega_c) + c_1 \cos(2\omega_c) + d_1 \cos(3\omega_c)}{1 + 2\alpha_1 \cos(\omega_c)}. \tag{3.12}$$

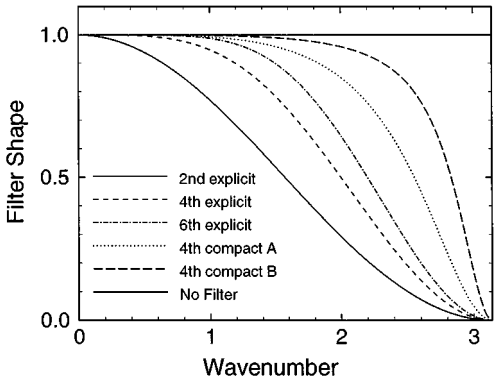

FIG. 9. Comparison of explicit and compact filters is shown as a function of wavenumber. Second-fourth- and sixth-order explicit filters remove more energy at lower wavenumbers than the two fourth-order compact filters (A and B) described in the text.

A family of fourth-order tridiagonal schemes is found when the constraints $T_c(\pi) = 0$, and $(dT_c/d\omega_c)(\pi) = 0$ are imposed. The coefficients for fourth-order accuracy are

$$a_1 = \frac{1}{8}(5 + 6\alpha_1 + 16d_1), \qquad b_1 = \frac{1}{2}(1 + 2\alpha_1 - 2d_1),$$
$$c_1 = \frac{-1}{8}(1 - 2\alpha_1 + 16d_1). \tag{3.13}$$

Wave reflection experiments were conducted using two different filter functions and the results were found to be approximately independent of the filter parameters. From inspection of various filters satisfying (3.13), the two that were utilized confine most of their effects below the $4\Delta x$ wave ($k\Delta x = \pi/2$). The first is represented by Filter A (4th-order compact) in Fig. 9 and may be written

$$0.4\check{u}_{i-1} + \check{u}_i + 0.4\check{u}_{i-1} = 0.4u_{i-1} + u_i + 0.4u_{i+1}$$
$$- \frac{1}{80}(u_{i+2} - 4u_{i+1} + 6u_i - 4u_{i-1} + u_{i-2}). \tag{3.14}$$

The second filter is confined even more strongly to high wave numbers and is represented by Filter B in Fig. 9. It is represented by

$$0.475\check{u}_{i-1} + \check{u}_i + 0.475\check{u}_{i+1} = 0.475u_{i-1} + u_i + 0.475u_{i+1}$$
$$- \frac{1}{320}(u_{i+2} - 4u_{i+1} + 6u_i - 4u_{i-1} + u_{i-2}). \tag{3.15}$$

Explicit fourth-order formulations are necessary for the boundary nodes of the filter. Formulations that exactly filter the $\omega_c = \pi$ waves are

$$\check{u}_1 = \frac{15}{16}u_1 + \frac{1}{16}(4u_2 - 6u_3 + 4u_4 - u_5), \tag{3.16}$$

$$\check{u}_2 = \frac{3}{4}u_2 + \frac{1}{16}(u_1 + 6u_3 - 4u_4 + u_5). \tag{3.17}$$

The three-dimensional version of (3.14), (3.15), or (3.9) is realized by performing three passes of the one-dimensional filters orthogonally. The compact filter is used in the x- and y-directions, and either the compact or the explicit filter is used on the variable grid (discussed below) in the z-direction.

3.3. *Time Differencing*

A major focus of the time-differencing scheme is to ensure that the flow satisfies the continuity equation. A third-order time accurate implementation of the projection method is utilized. The first-order accurate projection method was proposed independently by Chorin (1968) and Temam (1969) and extended to explicit time schemes by Fortin *et al*. (1971). The projection method and a family of related time discretization schemes are discussed in detail by Fletcher (1991), and appropriate boundary conditions are given by Kim and Moin (1985). Additional discussion of the projection method appears in Gresho (1990), and recent applications are presented by Karniadakis *et al*. (1991), Bell *et al*. (1989), and Rai and Moin (1991).

The projection method solves the momentum equations in two fractional steps. The first step forms an auxiliary flow field, $\mathbf{u}^*$, at the new time level by integration of the nonlinear, buoyancy, and dissipation terms. The second step then corrects the auxiliary flow field by applying the pressure gradient to guarantee incompressible flow.

An implementation of the first step of the projection method is illustrated here using third-order Adams–Bashforth time stepping:

$$\frac{\mathbf{u}^* - \mathbf{u}^n}{\Delta t} = \frac{23}{12}\left(-\mathbf{u}\cdot\nabla\mathbf{u} - \hat{k}\,Ri\,\rho + \frac{1}{Re}\nabla^2\mathbf{u}\right)^n - \frac{16}{12}\left(-\mathbf{u}\cdot\nabla\mathbf{u} - \hat{k}\,Ri\,\rho + \frac{1}{Re}\nabla^2\mathbf{u}\right)^{n-1} + \frac{5}{12}\left(-\mathbf{u}\cdot\nabla\mathbf{u} - \hat{k}\,Ri\,\rho + \frac{1}{Re}\nabla^2\mathbf{u}\right)^{n-2}. \tag{3.18}$$

It is followed by the projection step, in which $\mathbf{u}^*$ is projected onto its non-divergent subspace, $\mathbf{u}^{n+1}$, according to the relations

$$\frac{\mathbf{u}^{n+1} - \mathbf{u}^*}{\Delta t} + \nabla \bar{p}^{n+1} = 0, \tag{3.19}$$

$$\nabla\cdot\mathbf{u}^{n+1} = 0. \tag{3.20}$$

The appropriate pressure field for the projection step is formed by taking the divergence of (3.19) with the condition (3.20) and solving the resulting Poisson equation,

$$\nabla^2 \bar{p}^{n+1} = \frac{\nabla\cdot\mathbf{u}^*}{\Delta t}. \tag{3.21}$$

Boundary conditions for Poisson's equation of the Neumann type are obtained by using the component of (3.19) normal to the boundary, e.g., at $z = 0$,

$$\left.\frac{\partial \bar{p}}{\partial \mathbf{N}}\right|_B^{n+1} = -\frac{\left(\mathbf{u}_B^{n+1} - \mathbf{u}_B^*\right)\cdot\mathbf{N}}{\Delta t} = \left.\frac{\partial \bar{p}}{\partial z}\right|_B^{n+1} = -\frac{w_B^{n+1} - w_B^*}{\Delta t}. \tag{3.22}$$

The boundary values $\mathbf{u}_B^{n+1}\cdot\mathbf{N}$ are updated according to known boundary conditions, such as those appropriate for no-slip, free-slip, or periodic boundaries. The key to making (3.22) a stable boundary condition is correctly evaluating $\mathbf{u}_B^*\cdot\mathbf{N}$. Following Kim and Moin, (3.18) is solved at the boundaries using one-sided derivatives as if no true boundary condition were known. Thus, the auxiliary velocity field, $\mathbf{u}_B^*$, influences the determination of the pressure field at the boundary, which in turn influences the determination of the boundary velocity, $\mathbf{u}_B^{n+1}$, at the new time level. The projection step is completed by updating the boundary velocities to their prescribed values at each new time level to eliminate the buildup of roundoff and truncation errors.

In their discussion of the projection method, Peyret and Taylor (1983) state that, since the auxiliary velocity field appears both in the boundary condition for pressure (3.22) and Poisson's equation (3.21), it cancels identically, and therefore, a homogeneous boundary condition for pressure is sufficient. Chorin (1984) points out that their scheme is unstable and inconsistent. This inconsistency is demonstrated by Kim and Moin (1985). Gresho (1990) claims, however, that he has experienced no inconsistency using the homogeneous boundary condition, and discusses the two options in detail, giving preference to use of the simpler homogeneous boundary condition.

In the present work, the pressure field was found to be unstable when the homogeneous boundary condition was applied, and the instability became significant at long integration times. The numerical instability appears to depend on the type of physical velocity boundary conditions chosen. For a no-slip condition at the wall the instability was evident but very weak, and the time integration of the flow could be completed without significant loss of accuracy using the approximate homogeneous pressure boundary condition. For a free-slip boundary condition, however, the instability was too large to proceed with the approximate boundary condition. The probable cause is the relative magnitude of w_B^* for the two cases, because it is nearly zero for the no-slip wall but becomes much larger in the free-slip case. It may be that the disagreement in the literature as to the nature and effect of the instability arises from experiments conducted using differing physical boundary conditions. Fletcher (1991) adds that, for the closely related MAC method, the permissible use of $\frac{\partial \bar{p}}{\partial N}|_B = 0$ is specific to a particular second-order staggered grid spatial discretization, suggesting that other choices of numerical methods besides boundary conditions may also influence the strength and nature of the instability.

Karniadakis *et al*. (1991) demonstrate that the temporal treatment of the projection step is exact, and that the temporal accuracy of the overall method is determined only by the accuracy used for other terms in governing equations. They formalize the demonstration by writing the definition (following their nomenclature)

$$\nabla \bar{p}^{n+1} = \frac{1}{\Delta t} \int_{t_n}^{t_{n+1}} \nabla p \, dt. \tag{3.23}$$

Thus, the projection method is compatible with the explicit Adams–Bashforth scheme, except that the average pressure field, $\bar{p}^{n+1}$, is used to guarantee incompressible flow at the $n+1$ time level rather than a combination of the pressure fields p^n, p^{n-1}, p^{n-2} from earlier time levels.

From this view, advantages of the projection method become evident. The average pressure field $\bar{p}^{n+1}$ properly compensates for the truncation errors of the time and spatial discretization schemes that occur during the time integration, and thus the projection method is not susceptible to the accumulation of errors from the right-hand side of Poisson's equation in the same way as an explicit pressure treatment.

The projection method is implemented together with the third-order Adams–Bashforth (AB3) scheme. Startup of the simulation is done by using a forward Euler (AB1) time step for the first step and a second-order Adams–Bashforth (AB2) time step for the second time step. Advantages of the AB3 scheme, compared with several other time differencing methods, are discussed in Durran (1991). The main advantage of the AB3 scheme over more commonly used explicit second-order schemes, such as the leap-frog (L-F) method or the (AB2) scheme, is its stability. The leap-frog, (L-F) scheme is subject to a temporal oscillation of period $2\Delta t$. The second-order Adams–Bashforth (AB2) scheme has a weak unstable growth of order $(\Delta t)^3$ (Canuto *et al*., 1988, p. 102). In addition the AB3 scheme has smaller phase and amplitude errors than the AB2 or L-F schemes (Durran, 1991).

Greater efficiency is introduced in the model by using a variable time-stepping scheme that allows the time step to change based upon local and temporal stability criteria. (When a spatially variable grid is used, the local stability is proportional to the grid spacing, discussed below.) Gear and Watanabe (1974) demonstrate that variable time-stepping (multistep) methods have the same stability properties as the constant step Adams–Bashforth schemes

if the time step is changed in a relatively smooth fashion. Third-order accurate time stepping is maintained by integrating according to the relations

$$u_{n+1} = u_n + A_t \Delta t_1 \mathcal{F}^n + B_t(\Delta t_1 + \Delta t_2)\mathcal{F}^{n-1} + C_t(\Delta t_1 + \Delta t_2 + \Delta t_3)\mathcal{F}^{n-2}, \quad (3.24)$$

where Δt_1 is the time step between time level $n+1$ and n, Δt_2 is the time step between time level n and $n-1$, Δt_3 is the time step between time level $n-1$ and $n-2$, $\mathcal{F}^n$ represents the flux of u evaluated at time level n, and

$$A_t = 1 + \frac{\Delta t_1(2\Delta t_1 + 6\Delta t_2 + 3\Delta t_3)}{6\Delta t_2(\Delta t_2 + \Delta t_3)}, \quad (3.25)$$

$$B_t = \frac{-\Delta t_1^2(2\Delta t_1 + 3\Delta t_2 + 3\Delta t_3)}{6\Delta t_2 \Delta t_3(\Delta t_1 + \Delta t_2)}, \quad (3.26)$$

$$C_t = \frac{\Delta t_1^2(2\Delta t_1 + 3\Delta t_2)}{6\Delta t_3(\Delta t_1 + \Delta t_2 + \Delta t_3)(\Delta t_2 + \Delta t_3)}. \quad (3.27)$$

Figure 10 shows the actual time step used throughout a typical three-dimensional simulation. In the beginning of the simulation a constant time step fixed by the diffusion stability limit (D) is used (Subsection 3.4). After approximately time 30, the advection stability limit (A) is more restrictive, and the time step is adjusted so that the most severe Courant number criteria is held at a stable value of 99% of the maximum allowable value (according to criteria described below that includes a safety factor which is related to the aspect ratio of the nonuniform grid). This condition is typically encountered at the very fine mesh near the wall during the wave amplification process. By using the variable time step approach an efficiency of approximately 50% is saved. The calculation shown here took 12,000 time integration steps to complete, but if a constant time step ($\Delta t = 0.0075$) had been used that was small enough to maintain numerical stability throughout the simulation, the calculation would have taken over 18,000 time steps. Additional difficulty is avoided with the variable

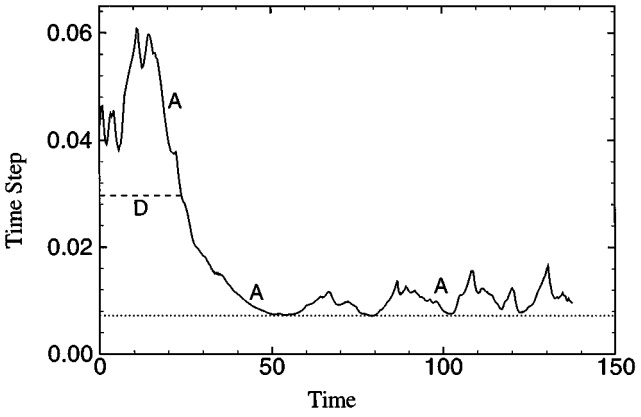

FIG. 10. The time step used in the numerical simulations is allowed to adjust during the simulation to achieve the largest stable time step during the transient process. The diffusion stability limit (D) is constant throughout the computation with a maximum stable time step of approximately 0.0295, which for the first 30 time units is the time step used. Line A is the stable value derived from the advection-buoyancy analysis given by Eq. (3.40). The advection stability limit becomes smaller than the diffusion limit after time 30 and varies throughout the calculation. Line D is made to follow the actual time step used in the simulation after time 30.

time step method, because *a priori* (before the simulation) the size of a sufficiently small (constant) time step is unknown. In contrast, in the variable time step approach, the flow field itself sets an economical stable time step.

3.4. *Numerical Stability Criteria*

The stability limits of the combined time and space differencing schemes for the nonlinear system may be approximated by performing a von Neumann stability analysis on the linearized system of governing equations. The numerical stability of the advection, buoyancy, and pressure terms are examined together and the stability of the diffusion terms is examined separately. This approach yields two separate necessary conditions for linear stability but does not guarantee sufficient conditions because the region of A-stability for third-order Adams–Bashforth approximation to $ds/dt = (a+bi)s$ is not a square in a plane with coordinate axes $a\Delta t$ and $b\Delta t$ (Gear, 1971). An approximate safety factor, described below, is used to convert the necessary conditions for the linear system (derived for a uniform grid) into sufficient conditions appropriate for the nonlinear system on a nonuniform grid. Following the approach of Durran (1992) limits on the maximum stable time step for the numerical simulation in the two-dimensional system are obtained. Again for simplicity we let $\alpha = 0$ and linearize the equations about a mean velocity $\bar{U}$, assumed constant,

$$\frac{\partial u}{\partial t} + \bar{U}\frac{\partial u}{\partial x} + \frac{\partial p}{\partial x} = 0, \tag{3.28}$$

$$\frac{\partial w}{\partial t} + \bar{U}\frac{\partial w}{\partial x} + Ri\,\rho + \frac{\partial p}{\partial z} = 0, \tag{3.29}$$

$$\frac{\partial \rho}{\partial t} + \bar{U}\frac{\partial \rho}{\partial x} - w = 0, \tag{3.30}$$

$$\frac{\partial u}{\partial x} + \frac{\partial w}{\partial z} = 0. \tag{3.31}$$

With Fourier component wave solutions for u, w, p, and ρ, of the form $u^n_{j_1,j_3} = \hat{u}e^{i(j_1 k\Delta x + j_3 m\Delta z - \omega_c n\Delta t)}$, where the grid point indices in the x- and z-directions are j_1 and j_3, respectively, and with leap-frog time stepping to illustrate the analysis, (3.28)–(3.31) may be written in wavenumber space as

$$\begin{bmatrix} -\sin\omega_c\Delta t + C_{fl}D_x & 0 & 0 & \frac{\Delta t}{\Delta x}D_x \\ 0 & -\sin\omega_c\Delta t + C_{fl}D_x & -i\,Ri\,\Delta t & \frac{\Delta t}{\Delta z}D_z \\ 0 & i\Delta t & -\sin\omega_c\Delta t + C_{fl}D_x & 0 \\ \frac{D_x}{\Delta x} & \frac{D_z}{\Delta z} & 0 & 0 \end{bmatrix} \begin{bmatrix} \hat{u} \\ \hat{w} \\ \hat{\rho} \\ \hat{p} \end{bmatrix} = \begin{bmatrix} 0 \\ 0 \\ 0 \\ 0 \end{bmatrix}, \tag{3.32}$$

where $C_{fl} = \frac{\bar{U}\Delta t}{\Delta x}$, $D_x = \Delta t/\Delta x \frac{3\sin(k\Delta x)}{2+\cos(k\Delta x)}$, and $D_z = \Delta t/\Delta z \frac{3\sin(m\Delta z)}{2+\cos(m\Delta z)}$.

For non-trivial solutions the determinant of the coefficient matrix must be zero, which leads to the condition

$$(-\sin\omega_c\Delta t + C_{fl}D_x)^2 = \frac{Ri\Delta t^2 D_x^2}{(\Delta x^2/\Delta z^2)(D_z/\Delta z)^2 + (D_x/\Delta x)^2}. \tag{3.33}$$

The right hand side has a maximum at $Ri\,\Delta t^2$, for all $0 \le k\Delta x \le \pi$ and $0 \le m\Delta z \le \pi$, and

so the stability criteria becomes

$$|-\sin\omega_c\Delta t| \geq |C_{fl}D_x + \sqrt{Ri}\Delta t|. \tag{3.34}$$

The maximum value of D_x is $\sqrt{3}$ at $k\Delta x = \frac{2\pi}{3}$; thus, for leap-frog time stepping, for $\omega_c\Delta t$ to be real valued, the stability criterion reduces to

$$\sqrt{3}\,C_{fl} + \sqrt{Ri}\Delta t \leq 1. \tag{3.35}$$

Adams–Bashforth third-order time stepping has a stronger stability restriction than the leap-frog scheme (see Durran, 1991). In this case it is required that

$$\sqrt{3}\,C_{fl} + \sqrt{Ri}\Delta t \leq 0.724. \tag{3.36}$$

This result has been verified experimentally.

In practice, $\Delta z < \Delta x$ and $\bar{U}$ varies throughout the domain. In this case, the forgoing analysis is modified to include a safety factor related to the most stringent stability restriction in the domain. Thus, we define $\bar{U}(x, y, z) = (u^2 + v^2 + w^2)^{1/2}$ as the local magnitude of the velocity field and seek the largest time step Δt that is stable at every location in the computational domain. For this we use

$$C_{fl} = \frac{\bar{U}(x,\ y,\ z)\,\Delta t}{\Delta z}, \tag{3.37}$$

and find the largest value of $\bar{U}(x, y, z)/\Delta z(z)$ in the computational domain on the variable grid (Subsection 3.6). While including the safety factor has the disadvantage of selecting a smaller advective time step than may be necessary for stability and therefore decreases the efficiency of the model, experience has always shown the model to be stable when following this procedure. In addition, there is a small advantage to taking smaller time steps than necessary because doing so increases the overall accuracy of the time discretization.

The diffusion term is treated explicitly with AB3 time stepping in this model. Other researchers have developed models that treat the diffusion term implicitly; e.g., Karniadakis *et al*. (1991) uses third-order Adams–Moulton time differencing. Implicit treatment of the diffusion term allows larger stable time steps. Experience has shown, however, that, for the problem being studied here, the nonlinear advection term has more restrictive stability criteria than the explicit treatment of the diffusion term. Thus, there is no clear advantage to using the more complicated implicit diffusion treatment.

The stability criteria for the diffusion terms are analyzed separately from the advection terms. This is done because of the simplicity of the analysis, the linearity of the diffusion terms, and because other factors of equal or greater importance (e.g., nonlinearity, nonuniform grid) have been neglected. The diffusion terms have different temporal properties from the advection terms and yield a second necessary condition for stability. Again for wave solutions, and with the discrete wavenumber representation for the second derivative from the compact scheme (Lele, 1992) the AB3 method yields the restriction

$$\beta = \frac{\Delta t}{Re\,\Delta z^2} \leq \frac{0.545}{6}. \tag{3.38}$$

This result is less restrictive than the time-lagged explicit treatment necessary for the leap

frog scheme, which yields $\beta \leq \frac{0.5}{6}$. The stability analysis for the density equation is equivalent, except that it requires a modified definition of $\beta_\rho = \frac{\Delta t}{Pe\,\Delta z^2}$.

3.5. *Numerical Boundary Conditions*

A wave-absorbing sponge layer is frequently used as an open boundary condition, e.g., Davies (1983) and Durran *et al*. (1993). In this model a sponge layer is used in the upper region of the finite computational domain. This layer is typically located far below the free surface of the fluid, and its purpose is simply to mimic the presence of the fluid above the computational domain. Rayleigh damping is an efficient wave-absorbing sponge layer, and is competitive with the best radiation boundary schemes for certain parameter ranges. The accuracy, however, is highly dependent upon the number of points used in the sponge layer. Durran *et al*. (1993) compare the wave absorbing layer to other wave permeable outflow boundary conditions. Typically, in the present model, ten percent of the total grid points ($\sim$13–40) are used to form the sponge layer. The damping coefficients are suggested by Klemp and Lilly (1978).

Rayleigh damping is of the form

$$\bar{\mu}_i = \mu_i - \sigma_i(\mu_i - \mu_{i0}), \tag{3.39}$$

where $\bar{\mu}$ is the damped value of an arbitrary function (such as $\mathbf{u}^*$ or ρ^{n+1}), μ is the predamped value, μ_{i0} is the relaxed value of the function in the sponge region (usually zero), and σ_i (discrete values of the damping coefficients at grid point i) is given for the present case by the Gaussian function

$$\sigma_z = e^{-\left(3.5 z_d / L_d\right)^2/2}, \qquad 0 \leq z_d \leq L_d, \tag{3.40}$$

where $z_d = z - (L_z - L_d)$ and L_d is the depth of the sponge layer (e.g., $L_z - L_d < z < L_z$). The two major disadvantages with the sponge layer are that it becomes computationally expensive if used at several open boundaries in a model, and it has the property that longer waves are absorbed less efficiently than short waves.

Additional complexity arises in the implementation of the sponge layer because it does not damp the flow in a non-divergent manner. The divergence is evident since the coefficients σ_i are functions only of z. This problem is solved by implementing the Rayleigh damping step before the projection step. In this manner the total damping procedure includes

$$\bar{u}_i^{n+1} = u_i^* - \sigma_i(u_i^* - u_{io}) - \Delta t \frac{\partial \bar{p}^{n+1}}{\partial z}, \tag{3.41}$$

where the value of the pressure gradient is determined from the projection method.

Neumann boundary conditions arise in the implementation of the zero flux boundary condition for density and for the free-slip velocity condition. The density boundary condition comes from (2.50), $\frac{\partial \rho}{\partial z}|_b = \cos\alpha$. The formula for third-order accuracy on a variable grid (see the following section) is

$$\rho_1 = \frac{-\Delta z_1 \Delta z_2 (\Delta z_1 + \Delta z_2)}{(\Delta z_1 + \Delta z_2)^2 - \Delta z_1^2} \cos\alpha + \frac{(\Delta z_1 + \Delta z_2)^2}{(\Delta z_1 + \Delta z_2)^2 - \Delta z_1^2}\, \rho_2 + \frac{\Delta z_1^2}{\Delta z_1^2 - (\Delta z_1 + \Delta z_2)^2} \rho_3, \tag{3.42}$$

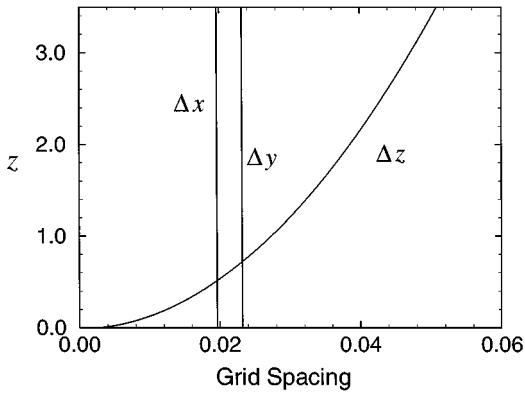

FIG. 11. The variable-mesh grid in the z direction Δz as a function of z. Also shown are the constant values of Δx and Δy, the grid spacings used in the x- and y-directions.

where Δz_1 is the distance between the locations of ρ_1 and ρ_2, and Δz_2 is the distance between the locations of ρ_2 and ρ_3. A free-slip condition $\frac{\partial u}{\partial z}|_b = 0$ is implemented with

$$u_1 = \frac{(\Delta z_1 + \Delta z_2)^2}{(\Delta z_1 + \Delta z_2)^2 - \Delta z_1^2}\, u_2 + \frac{\Delta z_1^2}{\Delta z_1^2 - (\Delta z_1 + \Delta z_2)^2}\, u_3. \tag{3.43}$$

3.6. *Variable Grid Spacing*

A variable-mesh grid is used to cluster computational nodes near the physical boundary at the ocean floor. An algebraic grid transformation from physical space (x, y, z) to the rectangular computational space (x, y, ζ), as shown in Fig. 11, is described here. The transformation is a function only of the z coordinate and is given by

$$z = a_\zeta \zeta + b_\zeta \zeta^2, \qquad 0 \le \zeta \le 1. \tag{3.44}$$

The inverse transform, $\zeta = G(z)$, is

$$\zeta = \frac{-a_\zeta}{2b_\zeta} + \sqrt{\left(\frac{a_\zeta}{2b_\zeta}\right)^2 + \frac{z}{b_\zeta}}. \tag{3.45}$$

The coefficients a_ζ and b_ζ are chosen so that the grid spacing closest to the wall, Δz_{min}, is about one tenth the grid spacing near the top of the domain Δz_{max}. For a three-dimensional realization with 130 grid points in the vertical, a typical choice employed is $a_\zeta = 0.4$ and $b_\zeta = 3.1$; results for Δz as a function of z are shown in Fig. 11. For a two-dimensional realization with 400 grid points in the vertical, a typical choice employed is $a_\zeta = 1$ and $b_\zeta = 2.5$.

The z-derivatives in the governing equations may be expanded by the chain rule, e.g.,

$$\frac{\partial u}{\partial z} = \frac{\partial u}{\partial \zeta}\frac{\partial \zeta}{\partial z}, \tag{3.46}$$

where

$$\frac{\partial \zeta}{\partial z} = \frac{1}{2b_\zeta \sqrt{(a_\zeta/2b_\zeta)^2 + z/b_\zeta}} = G_1(z) = \Gamma_1(\zeta) = \frac{1}{a_\zeta + 2b_\zeta \zeta}, \tag{3.47}$$

which yields

$$\frac{\partial u}{\partial z} = \Gamma_1(\zeta)\frac{\partial u}{\partial \zeta}. \tag{3.48}$$

By repeating this procedure $\frac{\partial^2 u}{\partial z^2}$ is obtained:

$$\frac{\partial^2 u}{\partial z^2} = \frac{\partial^2 u}{\partial \zeta^2}\left(\frac{\partial \zeta}{\partial z}\right)^2 + \frac{\partial u}{\partial \zeta}\frac{\partial^2 \zeta}{\partial z^2}. \tag{3.49}$$

With the definition

$$G_2(z) = \frac{\partial^2 \zeta}{\partial z^2} = \frac{-1}{4b_\zeta^2\left((a_\zeta/2b_\zeta)^2 + z/b_\zeta\right)^{3/2}} = \Gamma_2(\zeta) = \frac{-1}{4b_\zeta^2[\zeta + a_\zeta/2b_\zeta]^3}, \tag{3.50}$$

Eq. (3.49) may be written

$$\frac{\partial^2 u}{\partial z^2} = \Gamma_1^2(\zeta)\frac{\partial^2 u}{\partial \zeta^2} + \Gamma_2(\zeta)\frac{\partial u}{\partial \zeta}. \tag{3.51}$$

In addition, the fourth-order spatial filter requires the use of the term

$$\frac{\partial^4 u}{\partial z^4} = \Gamma_1^4(\zeta)\frac{\partial^4 u}{\partial \zeta^4} + 6\Gamma_1^2(\zeta)\,\Gamma_2(\zeta)\frac{\partial^3 u}{\partial \zeta^3} + \left[4\Gamma_1(\zeta)\,\Gamma_3(\zeta) + 3\Gamma_2^2(\zeta)\right]\frac{\partial^2 u}{\partial \zeta^2} + \Gamma_4(\zeta)\frac{\partial u}{\partial \zeta}, \tag{3.52}$$

where $\Gamma_3(\zeta)$ and $\Gamma_4(\zeta)$ are defined by

$$\Gamma_3(\zeta) = \frac{3}{8b_\zeta^3(\zeta + a_\zeta/2b_\zeta)^5}, \tag{3.53}$$

$$\Gamma_4(\zeta) = \frac{-3}{8b_\zeta^4(\zeta + a_\zeta/2b_\zeta)^7}. \tag{3.54}$$

Appendix B contains details concerning the fourth-order compact filter on the variable-mesh grid.

A motivation for choosing an algebraic grid transformation of this type is that the inverse transform may be determined exactly. To maintain fourth-order spatial accuracy in the mode, transformed derivatives such as $\frac{\partial \zeta}{\partial z}$ must be known to at least fourth-order accuracy. By choosing the algebraic transform given above, the derivatives for the transformation are known exactly, and the spatial accuracy is not compromised. Further discussion of these concerns and various approaches to resolving them may be found in Rai and Moin (1991). Alternative transforms are available that allow for higher-order clustering near the boundary. One such choice would be $z = a_\zeta \zeta^2 + b_\zeta \zeta^4$. Alternative, commonly used hyperbolic grid transforms are give in Anderson *et al*. (1984).

Applying these relations to the governing equations (2.13)–(2.17) and the pressure projection equation (3.21) leads to the modified set

$$\frac{\partial u}{\partial x}+\frac{\partial v}{\partial y}+\Gamma_1(\zeta)\frac{\partial w}{\partial \zeta}=0, \tag{3.55}$$

$$\frac{\partial u}{\partial t}+u\frac{\partial u}{\partial x}+v\frac{\partial u}{\partial y}+\Gamma_1(\zeta)w\frac{\partial u}{\partial \zeta}+Ri\,\rho\sin\alpha = -\frac{\partial p}{\partial x}+\frac{1}{Re}\left(\frac{\partial^2 u}{\partial x^2}+\frac{\partial^2 u}{\partial y^2}+\Gamma_1^2(\zeta)\frac{\partial^2 u}{\partial \zeta^2}+\Gamma_2(\zeta)\frac{\partial u}{\partial \zeta}\right)+F_u, \tag{3.56}$$

$$\frac{\partial v}{\partial t}+u\frac{\partial v}{\partial x}+v\frac{\partial v}{\partial y}+\Gamma_1(\zeta)w\frac{\partial v}{\partial \zeta} = -\frac{\partial p}{\partial y}+\frac{1}{Re}\left(\frac{\partial^2 v}{\partial x^2}+\frac{\partial^2 v}{\partial y^2}+\Gamma_1^2(\zeta)\frac{\partial^2 v}{\partial \zeta^2}+\Gamma_2(\zeta)\frac{\partial v}{\partial \zeta}\right)+F_v, \tag{3.57}$$

$$\frac{\partial w}{\partial t}+u\frac{\partial w}{\partial x}+v\frac{\partial w}{\partial y}+\Gamma_1(\zeta)w\frac{\partial w}{\partial \zeta}+Ri\,\rho\cos\alpha = -\Gamma_1(\zeta)\frac{\partial p}{\partial \zeta}+\frac{1}{Re}\left(\frac{\partial^2 w}{\partial x^2}+\frac{\partial^2 w}{\partial y^2}+\Gamma_1^2(\zeta)\frac{\partial^2 w}{\partial \zeta^2}+\Gamma_2(\zeta)\frac{\partial w}{\partial \zeta}\right)+F_w, \tag{3.58}$$

$$\frac{\partial \rho}{\partial t}+u\frac{\partial \rho}{\partial x}+v\frac{\partial \rho}{\partial y}+\Gamma_1(\zeta)w\frac{\partial \rho}{\partial \zeta}-w\cos\alpha-u\sin\alpha = \frac{1}{Pr\,Re}\left(\frac{\partial^2 \rho}{\partial x^2}+\frac{\partial^2 \rho}{\partial y^2}+\Gamma_1^2(\zeta)\frac{\partial^2 \rho}{\partial \zeta^2}+\Gamma_2(\zeta)\frac{\partial \rho}{\partial \zeta}\right)+F_\rho, \tag{3.59}$$

$$\frac{\partial^2 \bar{p}^{n+1}}{\partial x^2}+\frac{\partial^2 \bar{p}^{n+1}}{\partial y^2}+\Gamma_1^2(\zeta)\frac{\partial^2 \bar{p}^{n+1}}{\partial \zeta^2}+\Gamma_2(\zeta)\frac{\partial \bar{p}^{n+1}}{\partial \zeta}=\frac{1}{\Delta t}\left(\frac{\partial u^*}{\partial x}+\frac{\partial v^*}{\partial y}+\Gamma_1(\zeta)\frac{\partial w^*}{\partial \zeta}\right). \tag{3.60}$$

Two implications of using the variable grid deserve brief comment. For many numerical schemes there is appropriate concern about their order of accuracy, whether it be second-order, fourth-order, or spectral accuracy. The present model consistently maintains fourth-order spatial accuracy, meaning that the leading order error terms are $O(\Delta z^4)$. It should be realized, however, that when the grid spacing Δz changes by an order of magnitude across the domain, the absolute errors involved also may vary across the domain, in this example by relative magnitudes of up to 10^4. Consequently, grid clustering is an even stronger tool for achieving desired numerical resolution than using higher-order schemes. Standard finite-difference schemes use second-order accuracy, and some even use first-order spatial accuracy locally (e.g., the Total Variation Diminishing (TVD) scheme). This accuracy can be satisfactory if a high enough concentration of grid points is used. In the case of limited resources and marginally sufficient resolution, however, higher order schemes such as the compact scheme are very useful.

Our second comment addresses modeling turbulence is regions of high aspect ratios. In the present model the ratio of $\Delta x : \Delta z$ is approximately 5:1 at the wall. Other models use ratios of up to 100:1. A complication that may arise if the flow is turbulent in these regions is that gradients in z, adequately resolved in the high resolution direction, may be rotated (as by an eddy) into the low resolution direction and hence be unresolved. The use of high aspect ratio grids is justified when applied in regions of non-isotropic flows, such as in the viscous layer near a wall where high shears occur predominately in one direction.

3.7. *Pressure Solution*

Several methods have been examined to solve for the pressure field in the three-dimensional model in an efficient and accurate manner. The preferred solution method uses direct matrix inversions. This method is more accurate than iterative or multigrid techniques, eliminates the uncertainty of iterating subject to a convergence criteria, and requires less memory and CPU time. It is, however, limited to situations in which the problem has two directions of periodicity and uniform discretization. The governing Poisson equation,

$$\frac{\partial^2 p}{\partial x^2} + \frac{\partial^2 p}{\partial y^2} + \Gamma_1^2(\zeta)\frac{\partial^2 p}{\partial \zeta^2} + \Gamma_2(\zeta)\frac{\partial p}{\partial \zeta} = \frac{\nabla \cdot \vec{u}}{\Delta t} = R(x, y, \zeta), \tag{3.61}$$

is Fourier transformed in the x- and y-directions to form a set of separable equations for the pressure coefficients $\hat{\hat{p}}$

$$-k^2 \hat{\hat{p}} - l^2 \hat{\hat{p}} + \Gamma_1^2(\zeta)\frac{\partial^2 \hat{\hat{p}}}{\partial \zeta^2} + \Gamma_2(\zeta)\frac{\partial \hat{\hat{p}}}{\partial \zeta} = \hat{\hat{R}}(k, l, \zeta). \tag{3.62}$$

The modified Poisson equation is then solved for wave numbers k and l using explicit difference formulas for the ζ derivatives and the solution for the pressure coefficients $\hat{\hat{p}}(k, l, \zeta)$ is transformed back into physical space to obtain the pressure field. The implementation of this method also requires transforming the pressure boundary conditions.

The pressure solution has spectral accuracy in the horizontal directions and achieves fourth-order accuracy in the vertical direction by using five and four point stencils, respectively, as in (2.44), to estimate $\partial^2 p/\partial \zeta^2$ and $\partial p/\partial \zeta$. The method requires subsequent inversion of a pentadiagonal matrix of the form

$$\begin{aligned}\left(\frac{-\Gamma_1^2(i)}{12\Delta\zeta^2} + \frac{\Gamma_2(i)}{12\Delta\zeta}\right)\hat{\hat{p}}_{-2} + \left(\frac{4\Gamma_1^2(i)}{3\Delta\zeta^2} - \frac{2\Gamma_2(i)}{3\Delta\zeta}\right)\hat{\hat{p}}_{i-1} + \left(\frac{-5\Gamma_1^2(i)}{2\Delta\zeta^2} - k^2 - l^2\right)\hat{\hat{p}}_i \\ + \left(\frac{4\Gamma_1^2(i)}{3\Delta\zeta^2} + \frac{2\Gamma_2(i)}{3\Delta\zeta}\right)\hat{\hat{p}}_{i+1} + \left(\frac{-\Gamma_1^2(i)}{12\Delta\zeta^2} - \frac{\Gamma_2(i)}{12\Delta\zeta}\right)\hat{\hat{p}}_{i+2} = \hat{\hat{R}}(k, l, i),\end{aligned} \tag{3.63}$$

with special consideration required for the first two boundary nodes.

After the Poisson solver yields the pressure at every grid point, the pressure derivatives, $\frac{\partial p}{\partial x}$, $\frac{\partial p}{\partial y}$, and $\frac{\partial p}{\partial z}$ are formed using the compact scheme.

3.8. *Flow Visualization*

The complete velocity and density fields are stored regularly throughout the simulation to enable visualizations of the flow field at times of interest. Additional visualizations are made of the vorticity and stream-function fields.

A key issue related to wave breakdown is whether the turbulent boundary layer exchanges fluid with the interior domain, or whether it predominantly continues to mix the same fluid (Garrett, 1991a). Two additional features were added to the model experiments to study this issue. The first feature is the ability to track fluid particles. Particle trajectories are examined to determine if a statistically significant number of these particles escape from the boundary mixed layer, or if particles initially outside the boundary layer are entrained into it.

Sets of 2,000–10,000 Lagrangian particles are released in the flow in a rectangular lattice, after the flow has begun to develop. The equations describing their trajectories are time stepped using an Euler scheme with variable time steps. The fluid velocities $\vec{u}_p(x, y, z, t)$,

at the particle locations, $\vec{X}_p(x, y, z, t)$, are calculated using tri-linear interpolation, and then the particle locations are updated with the equation

$$\vec{X}_p^{n+1} = \vec{X}_p^n + \Delta t\, \vec{u}_p^n. \tag{3.64}$$

The particles are tracked for a number of wave periods and their locations are written every ten time steps. It is straightforward to modify the particle trajectory equation to include other effects on the particles (e.g., buoyancy, drag), thereby describing motion of particles whose trajectories differ from the local fluid motion (e.g., Maxey and Riley, 1983; Squires and Eaton, 1990).

A passive scalar field is also added in some of the simulations to observe net mass transport from one region to another. For the three-dimensional model a transport equation for the scalar quantity S_D is added to the system, e.g.,

$$\frac{\partial S_D}{\partial t} + u\frac{\partial S_D}{\partial x} + v\frac{\partial S_D}{\partial y} + w\frac{\partial S_D}{\partial z} = \frac{1}{Sc\,Re}\left(\frac{\partial^2 S_D}{\partial x^2} + \frac{\partial^2 S_D}{\partial y^2} + \frac{\partial^2 S_D}{\partial z^2}\right). \tag{3.65}$$

The new parameter in this equation is the Schmidt number, $Sc = \nu/\kappa_S$, the ratio of diffusivities for momentum and for the scalar. To maintain adequate resolution of scalar gradients, Schmidt numbers between 0.7 and 1.5 are used in the experiments, depending on the Reynolds number.

The scalar field behaves as a "dye," allowing observations of the transport of dyed fluid from the boundary layer region into the interior stratified domain. Initially the dye is released within the turbulent boundary layer after the flow has developed for a few wave periods and reached a quasi-steady state of mixing. The location of the dye is monitored as the flow develops through a number of wave periods.

3.9. *Energetics*

To understand the physical processes in the flow, its energetics are fundamental. Statistical quantities of interest are calculated during the simulation. Below are listed the equations for calculating the volume averaged kinetic energy (KE), potential energy (PE), total energy ($TE = KE + PE$), dissipation rate of kinetic energy (ϵ), dissipation rate of potential energy (χ), and buoyancy flux (BF), respectively,

$$KE = \frac{1}{2V}\int_V (u^2 + v^2 + w^2)\, dV, \tag{3.66}$$

$$PE = \frac{Ri}{2V}\int_V \rho^2\, dV, \tag{3.67}$$

$$\epsilon = \frac{1}{V}\int_V \frac{u}{Re}\left(\frac{\partial^2 u}{\partial x^2} + \frac{\partial^2 u}{\partial y^2} + \frac{\partial^2 u}{\partial z^2}\right) + \frac{v}{Re}\left(\frac{\partial^2 v}{\partial x^2} + \frac{\partial^2 v}{\partial y^2} + \frac{\partial^2 v}{\partial z^2}\right), + \frac{w}{Re}\left(\frac{\partial^2 w}{\partial x^2} + \frac{\partial^2 w}{\partial y^2} + \frac{\partial^2 w}{\partial z^2}\right) dV, \tag{3.68}$$

$$\chi = \frac{1}{V}\int_V \frac{Ri\,\rho}{Pr\,Re}\left(\frac{\partial^2 \rho}{\partial x^2} + \frac{\partial^2 \rho}{\partial y^2} + \frac{\partial^2 \rho}{\partial z^2}\right) dV, \tag{3.69}$$

$$BF = \frac{1}{V}\int_V Ri\,\rho(w\cos\alpha + u\sin\alpha)\, dV. \tag{3.70}$$

The wave forcing scheme of Subsection 2.3 adds energy to the flow at each time step. The total rate of work input W is the sum of the kinetic W_{KE} and potential W_{PE} energies added to the internal wave train, and may be calculated by the volume averages:

$$W_{KE} = \frac{1}{V}\int_V (uF_u + wF_w)\,dV, \tag{3.71}$$

$$W_{PE} = \frac{1}{V}\int_V Ri\;\rho\;F_\rho\,dV. \tag{3.72}$$

The flux of potential energy across the boundary is included in the dissipation term $\chi = Ri\,\rho\nabla^2\rho/(Pr\,Re)$, which includes both the dissipation and diffusion of potential energy. The net integrated diffusion is zero in the interior of the domain, but diffusive flux can be a source or sink across a physical boundary. Equations (3.77) below give an alternate method for determining χ. Several numerical simulations were conducted where dissipation was calculated using both (3.77) and (3.69). Typically, in the gravity wave reflection simulations, the magnitude of the diffusive flux of energy across the boundary was less than 1% of the dissipation rate, and the two curves were indistinguishable. Since it is much more efficient to calculate the two quantities together, as in (3.69), it is this approximate procedure that is generally followed.

The kinetic energy equation is a useful tool in examining flow development. For a control volume extending from the sloping wall up to the base of the sponge layer, the volume averaged kinetic energy equation can be obtained with the use of the divergence theorem. With this choice of the control volume, the dissipation of energy in the sponge layer is eliminated and replaced with terms representing the flux of energy across the control surface up into the sponge layer:

$$\frac{\partial KE}{\partial t} = \frac{1}{V}\int_V \left[-Ri\;\rho(w\cos\alpha + u\sin\alpha) + \epsilon + D_{f_{ke}} + W_{KE}\right] dV$$
$$+ \frac{1}{A_t}\int_0^{x_l}\int_0^{y_l} (w\cdot KE)|_{z=top}\,dx\,dy + \frac{1}{A_t}\int_0^{x_l}\int_0^{y_l} (w\cdot p)|_{z=top}\,dx\,dy, \tag{3.73}$$

where $D_{f_{ke}}$ is the dissipation-rate of kinetic energy by the filter, and A_t is the area of the top control surface.

The potential energy equation is derived by multiplying the density equation by ρRi and averaging over the computational domain.

$$\frac{\partial PE}{\partial t} = \frac{1}{V}\int_V \left[Ri\,\rho(w\cos\alpha + u\sin\alpha) + \chi + D_{f_{pe}} + W_{PE}\right] dV$$
$$+ \frac{1}{A_t}\int_0^{x_l}\int_0^{y_l} (w\cdot PE)|_{z=top}\,dx\,dy, \tag{3.74}$$

where $D_{f_{pe}}$ is the dissipation-rate of potential energy by the filter, and W_{PE} is the rate of work input of potential energy from the wave forcing mechanism. When added these equations form the total energy equation,

$$\frac{\partial TE}{\partial t} = \frac{1}{V}\int_V \left[\epsilon + \chi + D_{f_{ke}} + D_{f_{pe}} + W\right] dV$$
$$+ \frac{1}{A_t}\int_0^{x_l}\int_0^{y_l} [(w\cdot KE)|_{z=top} + (w\cdot p)|_{z=top} + (w\cdot PE)|_{z=top}]\,dx\,dy. \tag{3.75}$$

The energy and dissipation-rate spectra provide tools for examining nonlinearities and small-scale behavior of the flow. The spectra are straightforward to compute in planes parallel to the slope, because the flow field is known on a uniform (and periodic) grid. The vertical energy spectrum is determined by interpolating the velocity and density fields from the clustered grid onto a higher density uniform grid, e.g., from 400 grid points in the vertical to 1024 for the two-dimensional model or from 130 to 512 grid points in the three-dimensional model. Then the velocity fields are Fourier decomposed using a fast Fourier transform (FFT) package developed by Temperton (1983). Periodicity in the vertical direction is imposed by adding a mirror image of the flow field to the domain before decomposition. The final energy spectrum is formed from the Fourier wave amplitudes of the velocity fields by multiplying by their complex conjugates, dividing the result by two, and integrating these values over the domain.

The dissipation-rate spectra are formed by defining the viscous dissipation-rate function at every grid point. For a three-dimensional Newtonian, incompressible, viscous fluid the dissipation-rate function, Φ, is given by

$$\Phi = \frac{1}{Re}\left[2\left(\frac{\partial u}{\partial x}\right)^2 + 2\left(\frac{\partial v}{\partial y}\right)^2 + 2\left(\frac{\partial w}{\partial z}\right)^2 + \left(\frac{\partial v}{\partial x} + \frac{\partial u}{\partial y}\right)^2 + \left(\frac{\partial w}{\partial y} + \frac{\partial v}{\partial z}\right)^2 + \left(\frac{\partial u}{\partial z} + \frac{\partial w}{\partial x}\right)^2\right]. \tag{3.76}$$

The associated density (or potential energy) dissipation-rate function, and spectra are formed in like manner as

$$\chi = \frac{1}{Pr\,Re}\left[\left(\frac{\partial \rho}{\partial x}\right)^2 + \left(\frac{\partial \rho}{\partial y}\right)^2 + \left(\frac{\partial \rho}{\partial z}\right)^2\right]. \tag{3.77}$$

After the fields are formed they are interpolated onto a uniform mesh and Fourier decomposed. The amplitude of the complex Fourier wave components is integrated over the domain and plotted as the dissipation spectrum.

3.10. *Code Optimization*

To minimize in-core computer memory usage, as few data fields as feasible are stored at each time level. The approach used is to save the fluxes for the right hand side of the governing equations after every time step. The three-dimensional model, using third-order Adams–Bashforth time stepping, requires saving 12 flux fields (3 for each equation), 5 primitive variable fields, and 6 work arrays usually containing derivative fields to form the fluxes.

Particular attention has been paid during code development to allow the code to take advantage of increased performance speed achieved through vectorization and parallelization. The usual approach is to calculate for one plane at a time and to vectorize across the plane (i.e., while calculating values of $\frac{\partial u}{\partial x}$, the code is vectorized to calculate 128 derivatives for an entire y plane simultaneously). This approach is ideally designed for gains by parallelization of the code when ported to a parallel computer. Limited testing on a multi-processor Silicon Graphics Server shows that the code runs 3.9 times faster when run concurrently on 5 processors than when run on a single processor.

3.11. *Physical Parameters*

Following conventions, we define four different Reynolds numbers in the model. The first is the dissipation Reynolds number,

$$Re_d = \frac{\epsilon}{\nu N^2} \sim \frac{u^3}{\nu L N^2} = \left(\frac{uL}{\nu}\right)\left(\frac{u}{NL}\right)^2 \sim Re\, Fr^2, \tag{3.78}$$

which relates the dissipation rate of kinetic energy, ϵ, to the viscosity and buoyancy frequency. The second is the boundary layer Reynolds number,

$$Re_\delta = \frac{U_\infty \delta}{\nu}, \tag{3.79}$$

where U_∞ is the maximum velocity within the boundary layer, and δ is the boundary layer thickness. The third is the wave Reynolds number,

$$Re_w = \frac{C\lambda_z}{\nu} \sim \frac{\lambda N \lambda}{\nu} = \left(\frac{u\lambda}{\nu}\right)\left(\frac{N\lambda}{u}\right) \sim Re\frac{1}{Fr}, \tag{3.80}$$

which relates an approximate wave phase speed, C, and vertical wavelength, λ_z, to the viscosity. The last is simply the Reynolds number of the flow,

$$Re = \frac{U_w \lambda}{\nu}, \tag{3.81}$$

where U_w is the maximum current speed in the oncoming wave train, and $\lambda = 2\pi/|\mathbf{k}|$ is its wavelength.

From the simulations, typical values for these Reynolds numbers are

$$5 \le Re_d \le 200, \tag{3.82}$$

$$10 \le Re_\delta \le 200, \tag{3.83}$$

$$5{,}000 \le Re_w \le 40{,}000, \tag{3.84}$$

$$300 \le Re \le 4000. \tag{3.85}$$

In a similar fashion we define two Richardson numbers, the Richardson number $Ri = (N\lambda_z/U_w)^2$ based on the current velocity, and the wave Richardson number $Ri_w = (N\lambda_z/C)^2$ based on the phase speed C. Re_w and Ri_w are independent of the wave amplitude, A, while Re and Ri depend directly on A. Typical values for the Richardson numbers are $20 < Ri < 500$, while C is defined so that $Ri_w = 1$ in all of the experiments. Within the numerical model Re_w and Ri_w are used. Therefore the two key experimental parameters in the model are Re_w and A. Experimental results are normally presented in terms of Ri and Re which include the dependence on the wave amplitude.

It is important to note that the simulations are conducted at moderately low Reynolds numbers, far below values typical for oceanic conditions. The simulations are conducted at similar Reynolds numbers to those achieved in related laboratory experiments (though the simulations are at lower Richardson numbers). Typical oceanic internal waves may have Reynolds numbers of 10^7 based upon a length scale of 100 m, current speed of 10 cm/s, and kinematic viscosity of 10^{-6} m^2/s.

The present numerical methodology was not designed to include the full complexity of oceanic conditions, but rather to study the fundamental physics of the internal wave reflection problem. The goal is to seek qualitative and semi-quantitative information about physical processes that are not well understood. Important questions regarding the dependence on the Reynolds number, and effects of other oceanic flow features, are not accessible within the present approach. Since the internal wave reflection does not appear to be microscale driven, however, small-scale turbulence and viscosity do not dominate or invalidate the useful information derived from the results. Here, the role of turbulence and small scale features is primarily to dissipate internal wave energy. The present model, with its inherent limitations, serves as a useful starting point for numerical studies of internal wave reflection.

Several additional dimensional and dimensionless parameters are used in the simulations, and some typical values are listed here. Physical constants for gravity and background density are

$$g = 9.8 \text{ m/s}, \qquad \rho_o = 1000 \text{ kg/m}^3. \tag{3.86}$$

In turbulent simulations it is often necessary to have the diffusivity of density greater than the diffusivity of momentum to adequately resolve strong density gradients throughout the time integration. It is generally agreed that Prandtl number relating turbulent eddy viscosity coefficients for density and momentum should be of order 1; so we choose

$$0.6 \leq Pr \leq 1. \tag{3.87}$$

For the problem to be periodic in x the width of the domain L_x is set to an integral number of wavelengths (typically, $n = 1$ or $n = 2$) appropriate to $L_x = n\lambda_x$. Typically, small values of the bottom slope $0 \leq \alpha \leq 30^\circ$ and angle of wave propagation $3 \leq \theta \leq 30^\circ$ are of interest. A set of physical parameters, chosen in the mid-range of velocity and stratification appropriate for this study, leads to the set of model parameters

$$Re_w = \frac{(10^{-1} \text{ m/s})(10 \text{ m})}{10^{-4} \text{ m}^2/\text{s}} = 10{,}000, \tag{3.88}$$

$$Ri_w = \left[\frac{(10^{-2} \text{ s}^{-1})(10 \text{ m})}{10^{-1} \text{ m/s}}\right]^2 = 1, \tag{3.89}$$

$$Pe = Re. \tag{3.90}$$

This set of nondimensional parameters has been used in well-resolved, direct numerical simulations of the gravity wave reflection problem.

3.12. *Running the Experiments*

This section presents a brief description of how the numerical experiments are monitored and adjusted throughout the computations. After choosing the parameters for each three-dimensional simulation the flow is initialized with white noise in the lower half of the domain as described in Subsection 2.5. On a low resolution grid of $65 \times 33 \times 130$ (x, y, z) grid points, the noise is then allowed to adjust for one to two buoyancy periods into low-level, stratified turbulence exhibiting coherent structures. At this point the wave forcing mechanism is turned on in the top half of the domain and the waves begin to propagate

downward towards the wall in a somewhat linear fashion. During this transient stage of the calculation, no additional resolution is required to resolve the developing flow field.

Typically after four to five buoyancy periods, the leading edge of the wave train reaches the bottom slope. By this time the energy in the noise near the boundary has typically died away by roughly an order of magnitude, from its initial level to a weak background perturbation field. At this time the energy density level in the noise field is approximately one to five percent the energy density of the oncoming wave. After two to three more buoyancy periods, the flow starts to exhibit nonlinear behavior as the wave reflection process begins to strengthen. A typical flow feature observed during this stage is a strong density gradient developing in the boundary layer region. At this stage of flow development the simulation is moved onto a higher resolution numerical grid. The process of regridding is done by using Fourier interpolation, for example, onto a $129 \times 33 \times 130$ grid point mesh.

During the next wave period it usually becomes apparent if the flow will develop into turbulence or remain laminar. The turbulent cases often required further regridding onto more refined grids to resolve the three-dimensional structures that developed in the boundary layer. This is also done by Fourier interpolation in the y-direction, onto grids of either $129 \times 65 \times 130$, or when warranted $129 \times 129 \times 130$, depending upon the physical dimensions of the problem and resolution criteria. The grid clustering in the z-direction is not changed during the simulations, but rather is set at the beginning to a degree that will adequately resolve the boundary layer (based upon experience).

After regridding to the highest resolution for the simulation, the flow is run out for 10 to 30 more buoyancy periods (roughly 10,000 to 50,000 times steps). This typically allows a quasi-steady flow pattern of wave reflection and breakdown to develop and be recorded. The resolution requirements are determined by a number of factors. These include analysis of the energy spectrum as discussed above, comparisons of the energy removed at well-resolved scales and by the scale-dependent filter, and determination of whether a direct numerical or large eddy simulation is being conducted. Some of the numerical simulations may be considered a hybrid between direct numerical and large eddy simulations. This may be the most appropriate description for cases in which approximately 80% of the energy is dissipated at well-resolved scales by the true molecular effects (e.g., through the kinetic energy dissipation rate) and approximately 20% of the energy is dissipated by the hyperviscosity filter at the smallest scales on the numerical mesh. In these cases, it is expected that the small degree of subgrid-scale dissipation does not significantly affect the development of the flow at the large, energy-containing scales of motion.

The three-dimensional simulations are computationally expensive and time consuming. The high resolution runs (at $129 \times 129 \times 130$ grid points) take approximately 24 hours of CPU time on the Cray-YMP to complete 4500 time steps. The code is written in portable FORTRAN 77, and the simulations have been conducted without modification on six platforms including Stardent, Hewlett-Packard, DEC, Cray, SGI, IBM, and Sun servers, supercomputers and workstations. A simulation at a resolution of $129 \times 65 \times 130$ requires approximately 110 megabytes of memory using single precision on a 32-bit workstation. It takes about two minutes of CPU time per time step on a HP-9000 series 715 workstation, or 9 seconds of CPU time per time step on the Cray-YMP. Frequently, to make the best use of computer resources, the low resolution portions of the simulation were conducted on the local workstations and then restarted on the Cray computers after regridding for the turbulent portions of the simulation.

3.13. *Summary*

The numerical models developed herein provide state-of-the-art computational techniques for simulating incompressible, stratified flows. These models include several new features, such as the wave forcing mechanism and the combination of variable time-stepping with the third-order Adams–Bashforth projection method. The models are designed for accuracy and, when used at low Reynolds number, represent a direct numerical simulation (DNS) of a turbulent boundary layer. At higher Reynolds number the model may be considered a large eddy simulation (LES) of the flow, with a simple hyperviscosity filter used to dissipate energy from the subgrid scales of motion. The majority of the simulations conducted for this study are direct numerical simulations. In the following section results of DNS and LES simulations are presented. The gravity wave reflection problem for which the code was designed illustrates the capabilities of the numerical model and permits insightful analyses of the physics of the flow.

4. RESULTS

This section contains results from the computational experiments. Several high resolution simulations have been conducted (Slinn, 1995) to investigate internal wave reflection and are reported elsewhere (Slinn and Riley, 1996, 1998a, 1998b). These experiments used oncoming waves of moderate amplitudes from the mechanical wave forcing scheme and were designed to observe nonlinear interactions that occur in the bottom boundary layer. Additional two-dimensional simulations and linear analyses were used for comparison, and to help understand the influence of nonlinearity and three-dimensional interactions. Here, results from DNS and LES examples of internal wave reflection will be described, but first a brief description of the model-validation methods is given.

4.1. *Model Validation*

A variety of methods were used to validate the code and to gain confidence in the accuracy of the numerical experiments. These fall into four categories: (1) comparison with analytical solutions, (2) internal consistency checks, such as conservation of mass, momentum, and energy, (3) comparison with experiments, and (4) meeting established resolution criteria.

The flow field explained by Phillips (1970) and presented in Subsection 2.6 provides an analytic solution available for testing the accuracy of the code in two ways. The first test was simply to initialize the model with the Phillips' boundary layer velocity and density profiles. This test was done to see if the flows remained steady for a variety of boundary layer Reynolds, Richardson, and Prandtl numbers, as well as for different bottom slopes. The codes passed these simple tests, which were also valuable for determining how many grid points are required near the wall to adequately resolve the buoyancy driven flows as a function of the Reynolds number.

The second validation technique involving the Phillips' solution was a transient test. The model was initialized with no flow and a linear density gradient extending to the wall. At time zero the flow was allowed to start from rest by applying the zero-flux boundary condition (2.50) on the density field. This forced the flow towards the steady state solution. Parameters for this case are $Re_\delta = 13$, $Re_w = 10{,}000$, $Ri_w = 1$, $Pr = 1$, and $\alpha = 9.22^\circ$. The energetics of the transient test are illustrated in Fig. 12. The transient tests indicated that it took about two buoyancy periods for the boundary layer profiles to overshoot the energy

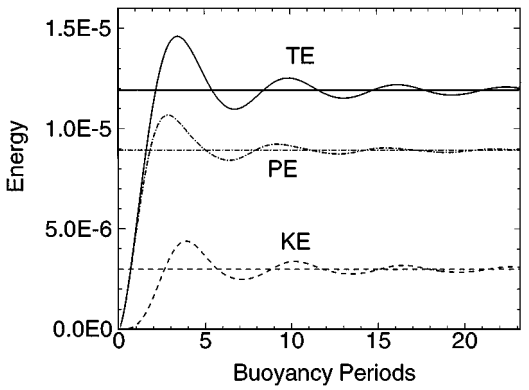

FIG. 12. Kinetic, potential, and total energy integrated over the control volume for the transient Phillips' test. The steady state values for energy are plotted for comparison.

in the steady solutions. The kinetic energy in the transient case reached about 1.5 times the kinetic energy of the steady flow before rebounding toward the steady solution. The transient solution exhibited damped oscillations about the steady solution with a period of about six buoyancy periods. After approximately 20 buoyancy periods the variations in the transient solution had decayed, and the flow nearly achieved the steady state predictions. The magnitude of the oscillations, at the last times in this experiment, were less than 5% of the energy in the steady solution. For comparison, the wave period of a critical frequency wave for the bottom slope, 9.2°, is approximately 6 buoyancy periods. The response time scale of the buoyancy boundary layer is shorter than the convective or wave propagation time scales associated with the overall wave reflection process. These results are typical of tests at different slopes, between 5° and 30°; however, very shallow slopes have slower response times. The buoyancy boundary layer is restricted to a thin region near the wall, and the energy density there is much less than that contained in the finite amplitude gravity waves used in the numerical simulations.

Code validation was also investigated by studying some of the simplest wave reflection problems, for which linear theory and intuition provide pictures of the flow behavior. One such case is the reflection of internal waves of small amplitude from a flat bottom. Here the oncoming wave is expected to reflect from the bottom without changing wavelength. In addition the interactions between the oncoming and outgoing wave trains are expected to be minimal, so that they simply add constructively (while passing through one another). The test was successfully completed. A steady flow was achieved as the oncoming wave train reflected from the bottom boundary, without changing wavenumber or frequency, and passed through the incident wave train without event, ultimately progressing into the upper sponge layer where the wave energy was absorbed without significant reflection.

A fourth test, allowing direct comparison with linear theory, examined vertical spectra of small amplitude waves reflecting from sloping boundaries. Provided the waves are somewhat removed from the critical angle, linear theory predicts the vertical wavenumbers of the reflected waves. Analysis of the energy spectra of the computed flow shows the transfer of energy to the predicted higher wavenumber. In this way it is straightforward to identify the energy associated with the oncoming and the reflected wave trains.

The effect of the sloping bottom is to increase the energy density of the reflected wave. Using linear theory, Phillips (1977) predicts, for the ratio of the reflected to incident wave

amplitude and energy density, respectively,

$$\frac{A_r}{A_i} = \frac{\cos(\alpha - \pi + \theta)}{\cos(\alpha + \pi - \theta)}, \tag{4.1}$$

$$\frac{E_r}{E_i} = \left(\frac{A_r}{A_i}\right)^2. \tag{4.2}$$

To obtain the wavenumbers of the reflected waves, it is necessary to use linear theory predictions in the rotated coordinate system (x, z). In the unrotated (x_T, z_T) coordinate system, $k_{Tr}/m_{Tr} = k_{Ti}/m_{Ti}$ and

$$\frac{m_{Tr}}{m_{Ti}} = \frac{A_r}{A_i} = A_F, \tag{4.3}$$

where A_F is the amplification factor. In the rotated coordinate system, however, $\lambda_{xi} = \lambda_{xr}$, or equivalently $k_r = k_i$, and thus all change in wavelength is observed in the z direction. The ratio m_r/m_i may be determined by considering the relationships

$$k_T = k\cos\alpha - m\sin\alpha, \tag{4.4}$$

$$m_T = k\sin\alpha + m\cos\alpha, \tag{4.5}$$

$$k = k_T\cos\alpha + m_T\sin\alpha, \tag{4.6}$$

$$m = -k_T\sin\alpha + m_T\cos\alpha. \tag{4.7}$$

Algebraic manipulation between the reference frames leads to theresults

$$\frac{m_{Tr}}{m_{Ti}} = \frac{k_r\sin\alpha + m_r\cos\alpha}{k_i\sin\alpha + m_i\cos\alpha} = A_F, \tag{4.8}$$

$$\frac{m_r}{m_i} = A_F\left[\frac{k_i\sin\alpha + m_i\cos\alpha}{\cos\alpha}\right] - \frac{k_i\sin\alpha}{\cos\alpha}, \tag{4.9}$$

$$\frac{k_r}{k_i} = 1. \tag{4.10}$$

Figure 13 shows the vertical kinetic energy spectra for a small amplitude wave train, with amplitude approximately $A = A_0/30$ (where A_0 is the amplitude of an overturning wave) and frequency 0.16, which has reflected from a bottom slope of 5°. This case was run at

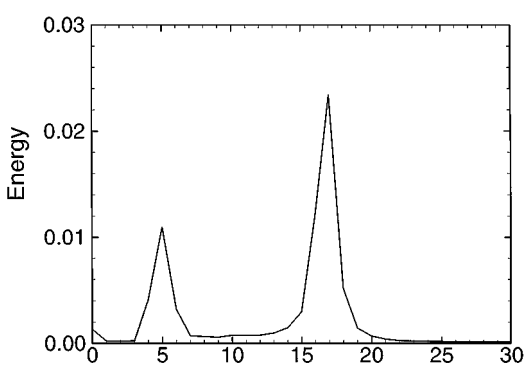

FIG. 13. Kinetic energy spectra in the vertical direction for a linear amplitude wave train reflecting from a sloping boundary with a no-slip boundary condition.

$Re = 2350$ with a no-slip bottom boundary condition, and (at the time shown) reached a quasi-steady state. Here the oncoming wave train has a wavenumber m_i of 5, and linear theory predicts an amplification factor $A_F = 3.3$ with a reflected wavenumber m_r (in the z-direction) of 17.1 for the inviscid case. Note that the reflected peak contains approximately twice as much energy as the oncoming wave train, consistent with the linear (inviscid) relationships, even though significant dissipation has occurred in the model. The results are thus in reasonable agreement with predictions. Experiments with somewhat larger amplitude linear wave reflection (Slinn, 1995) show the development of an intermediate peak at a wavenumber of approximately 11.5 that appearsto be related to resonant triad interactions (Thorpe and Haines, 1987).

To predict flows accurately the numerical model must satisfy the governing physical laws. The code was checked for internal consistency to ensure that it conserves mass, momentum, and energy. The conservation of mass for an incompressible flow is represented by the continuity equation $\nabla \cdot \mathbf{u} = 0$. Two measures of the divergence of the flow are monitored during the simulations: local and global divergence. The global divergence criterion in the three-dimensional model compares the volume integrals of $\int_V (\frac{\partial u}{\partial x} + \frac{\partial v}{\partial y})^2 \, dV$ and $-\int_V (\frac{\partial w}{\partial z})^2 \, dV$. For all of the experimental results the global divergence is negligible. Typically the ratio of

$$\frac{\int_V (\partial u/\partial x + \partial v/\partial y)^2 + (\partial w/\partial z)^2 \, dV}{\int_V (\partial w/\partial z)^2 \, dV} \tag{4.11}$$

is less than $1/10^4$ during periods of strong turbulence. At the beginning of the simulations when the flow is laminar and the waves are approaching the wall, the flow is incompressible to one part in 10^5, approximately the same magnitude as roundoff errors in single precision calculations.

The local divergence criterion is a normalized measure that gives the magnitude and location of the largest divergence in the model. The maximum of the local divergence is normalized by the mean shear at each vertical level, z, e.g.,

$$\overline{\frac{\partial u}{\partial x}}(z) = \frac{1}{L_x L_y} \left(\int_A \left(\frac{\partial u}{\partial x} \right)^2 dx \, dy \right)^{1/2} (z), \tag{4.12}$$

and is calculated by $\nabla \cdot \mathbf{u} / \overline{\frac{\partial u}{\partial x}}$. For a large number of simulations the largest local divergence consistently occurred near the wall. Usually this occurred at the third or fourth grid point from the wall, in the region where Δx is three to five times larger than Δz (associated with the variable grid). A typical maximum local divergence is about 1%. The fact that the divergence is small and is located in a region where it might be expected (because special treatment is used to resolve strong gradients in the z direction) builds confidence in the accuracy of the model results. The model conserves mass to acceptable tolerances.

Every simulation provides information about the balance of energy for the flow. All of the terms of the kinetic, potential, and total energy equations are calculated at each tenth time step during the simulations. The terms are summed and graphed to ensure that energy is conserved. The energy balance requirement is a more severe test of the accuracy of the model than either conservation of mass or momentum, because the energy terms are calculated using higher-order spatial derivatives. The kinetic energy balance is shown in Fig. 14 for a turbulent wave reflection experiment with Reynolds and Richardson numbers (based upon the wavelength and maximum current speed of the oncoming wave) of $Re = 1100$ and

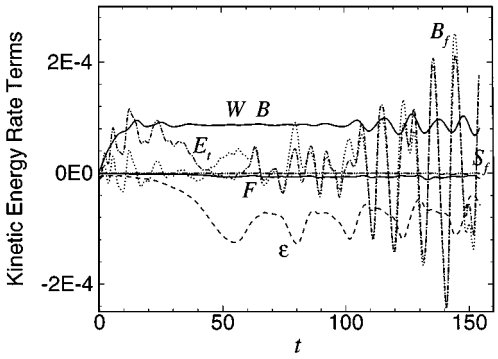

FIG. 14. Kinetic energy balance for a turbulent wave breakdown case, showing the degree of energy conservation in the model. Terms are labelled as work input (W), bouyancy flux (B_f), time rate of change of energy (E_t), balance (B), sponge flux (S_f), dissipation rates (ϵ and χ), and filter losses (F).

$Ri = 110$. In this case $Pr = 1$ and the bottom slope and angle of wave propagation are equal, $\alpha = \theta = 20^\circ$, so that this is a critical angle experiment. The energy conservation illustrated in Fig. 14 is typical for the turbulent simulations. The largest terms in the energy equations are the input of work (W) and the dissipation of energy (ϵ and χ). For the kinetic and potential energy equations, the buoyancy flux (B_f) is also quite large and oscillates throughout the simulation.

The sum of all of the energy terms would yield a balance term (B') that is approximately equal to zero. It was preferable not to plot the balance term B' near the zero line because it was difficult to distinguish from other small energy terms, such as the fluxes of energy into the sponge layer. Therefore we chose to plot the sum of all of the energy terms except for the work input, and show it by a balance curve (B), which should be equal to the work input (W) curve when energy is conserved. Kinetic, potential, and total energy are conserved to a high degree of accuracy.

The last type of internal consistency check is comparison between the two- and three-dimensional models. Some of the three-dimensional calculations were repeated in two dimensions to provide a comparison, to study the three-dimensional characteristics of the flow, and to check relationships between accuracy and resolution. The two-dimensional simulations were typically well-resolved at grid resolutions of 201×400.

Additional code validation comes from comparison with laboratory experiments of similar flows. Cacchione and Wunsch (1974), Taylor (1993), and Ivey and Nokes (1989) have studied the critical angle reflection. There were some features of their laboratory setup that are not exactly duplicated by the numerical model. One difference is the method of wave generation. The model uses an oncoming wave train, whereas (because of the tank geometry) the laboratory experiments used a mode-one internal wave that has vertical wavelength equal to the depth of the fluid. The laboratory experiments were also conducted at somewhat higher Reynolds and Richardson numbers than attainable with direct numerical simulations, although both were well within the range for turbulent wave breakdown to occur.

Close agreement exists between the laboratory and numerical experiments in the cases where similar experiments are available (Slinn, 1995). The two flows go through the same quasi-periodic behavior, with qualitatively similar flow features developing at each stage of the cycle. This builds confidence for additional numerical results for which no laboratory experiments have been conducted. The numerical experiments have the advantage of being

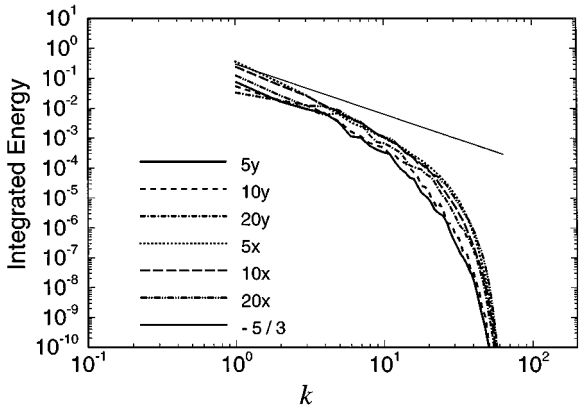

FIG. 15. Horizontal energy spectrum from a three-dimensional calculation as a function of horizontal wavenumbers k (or l). There are 6 energy curves in the figure, three energy spectra decomposed in the x-direction, labeled $5x$, $10x$, and $20x$, and three energy spectra decomposed in the y-direction, labeled $5y$, $10y$, and $20y$. They are at heights $z = 0.019$, 0.052, and 0.15, respectively, corresponding to the 5th, 10th and 20th grid points from the bottom boundary. Also shown is a reference line with a slope of $k^{-5/3}$.

able to study cases not accessible to laboratory experiments. For example, small bottom slopes (which are common in oceanic applications) have been difficult to simulate in the laboratory.

The final code validation method to be discussed is a check of numerical accuracy. When a direct numerical simulation is resolved satisfactorily, it gives the correct solution; e.g., increasing the resolution significantly and repeating the simulation does not alter the results materially. A standard method to determine if a simulation is resolved satisfactorily is to examine the energy spectra. A well-resolved spectra will contain significantly less energy at higher wave numbers (small scales) than at the low wave numbers (large, energy-containing scales). A rule-of-thumb for the DNS of turbulence is that the energy level at the largest scales should be approximately three orders of magnitude higher than that at the smallest scales of motion.

The average horizontal energy spectra on three different x-y planes are shown in Fig. 15 from an experiment with parameters $\alpha = \theta = 30^\circ$, $Re = 1700$, $Ri = 138$. Each of the spectra is taken in the turbulent boundary layer region, at $t = 79.5$ (five wave periods after startup) at distances from the wall of $z = 0.019$, 0.052, and $0.15\lambda_z$, respectively. At this stage the flow has reached a quasi-steady turbulent state. The horizontal spectrum gives a good measure of the resolution of the simulation, without adding the complication of interpreting the spectrum on the variable grid. The flow was computed on a $128 \times 128 \times 130$ grid; therefore, the highest horizontal wavenumber on the mesh is 64. The region of wavenumber space above $k = 40$ is strongly influenced by the removal of energy by the compact filtering. Also shown is a reference line with a slope of $k^{-5/3}$. The aspect ratio $\Delta x/\Delta y = 1.1$ is very close to one; therefore, the spectra in the x- and y-directions are considered together. Figure 15 indicates that the flow was well-resolved with a strong roll-off of energy at higher wavenumbers. There are approximately four orders of magnitude more energy in wavenumbers between 1–5 than in wavenumbers between 20–30 which are not significantly affected by the compact filter.

The overall consistency of the validation tests (with linear theory, comparison with laboratory data, conservation properties, and internal numerical tests), together with the physical

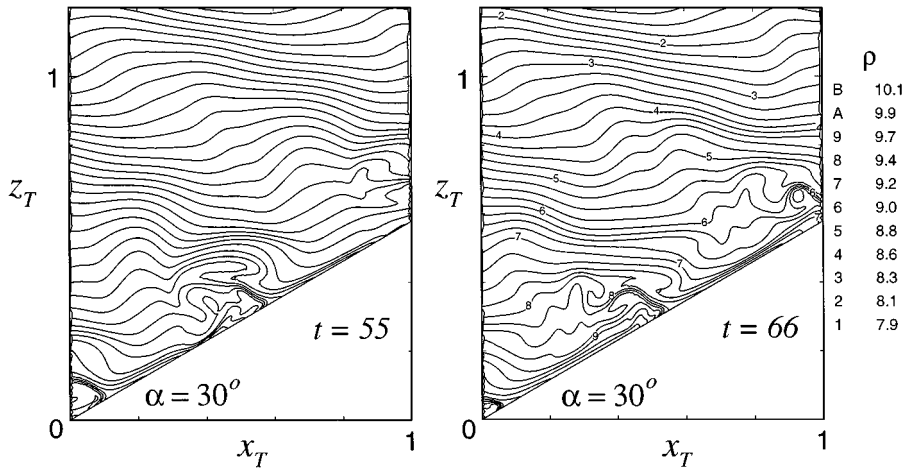

FIG. 16. Density fields in an x-z plane in the near wall region for critically reflecting internal waves from a bottom slope of 30°.

coherence of the results, Slinn and Riley (1996, 1998a, 1998b), allows confidence that the model accurately represents the fundamental physics of the flows.

4.2. *Critical Reflection Experiment*

Throughout the remainder of this section, the capabilities of the model are illustrated as concepts about wave reflection and boundary layer development and are examined from a numerical simulation. The bottom slope in this experiment is $\alpha = 30^\circ$, $Re = 1000$, $Ri = 108$, and $Pr = 1$. The fundamental frequency of the oncoming wave ($\omega = 0.5$) is chosen so that, upon the wave's reflection, the angle of the group velocity vector to the horizontal matches the bottom slope, *i.e.*, the wave is at the critical angle. It is representative of cases where transition to turbulence occurs during wave breakdown. Figure 16 shows isopycnals from a two-dimensional cross-section from the experiment in the near wall region at $t = 55$ and 66, where time is nondimensionalized by the buoyancy frequency, N, the wave period is 12.56, and the buoyancy period is 2π. The oncoming wave train is of moderate amplitude and regions of wave overturning and strong density gradient have developed near the bottom boundary. Here an arbitrary constant background density field $\rho_0 = 10$ has been added to the mean density gradient and fluctuations, consistent with the Boussinesq approximation. Only the lower portion of the computational domain to a height of $1.2\lambda_z$ is shown in the figure (the full domain is $3\lambda_z$ high), thus emphasizing the near-wall region. The dimensions are normalized by λ_z and there are two horizontal wavelengths in the x-direction, $\lambda_x = 0.577\lambda_z$. The model is periodic in the y-direction with the width of the domain set at $L_y = 0.6\lambda_z$.

By time $t = 30$, the wave train has reached the wall, and a strong gradient in density has formed. This feature, called a thermal front by Thorpe (1992), moves upslope at the x component of the phase speed of the oncoming wave. As time progresses, wave overturning develops in the lee of the thermal front, and at time $t = 55$, statically unstable fluid is apparent. As time continues, the overturned regions break down into small-scale turbulence and dissipate the wave energy in a three-dimensional fashion. Here the flow appears to be quasi-steady, with a locally turbulent region of statically unstable fluid moving upslope together with the thermal front. This result supports the observations of Ivey and

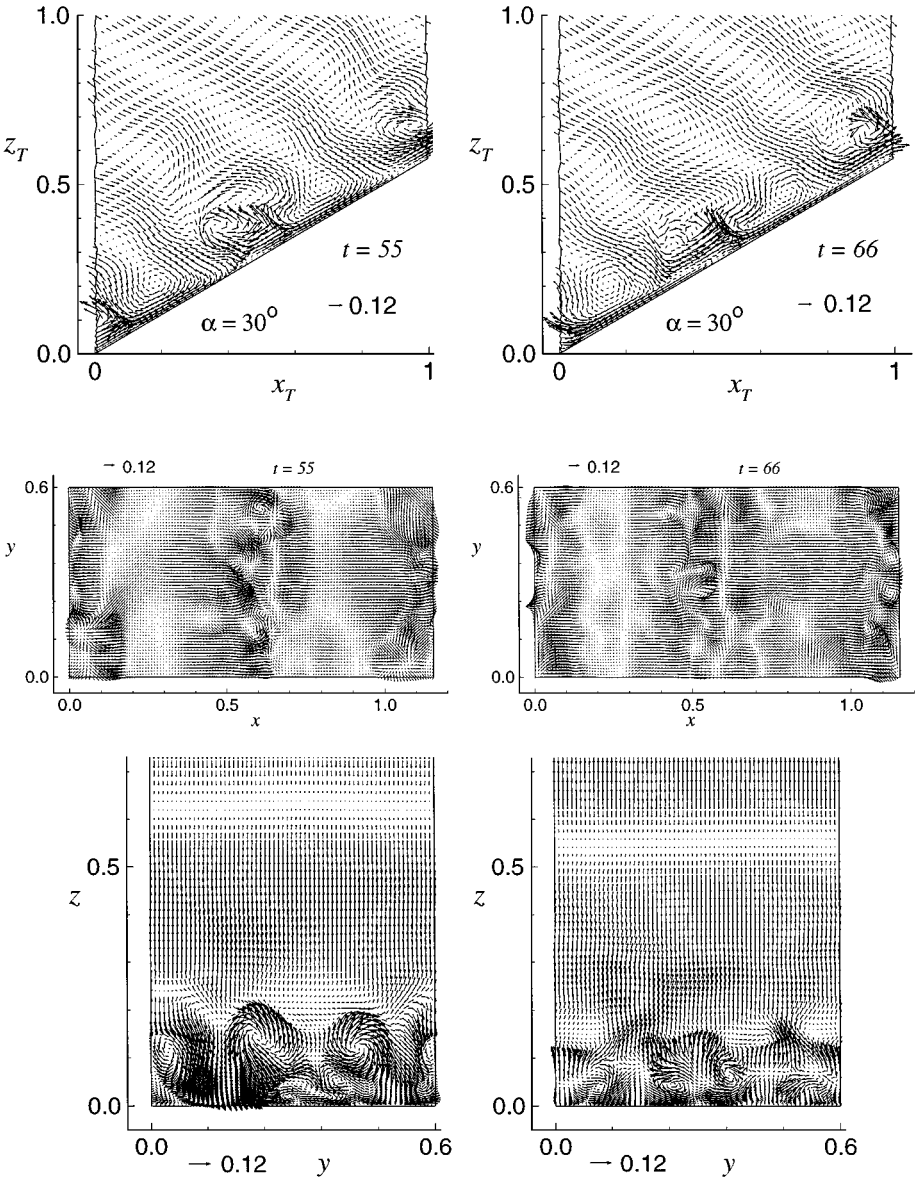

FIG. 17. Velocity vectors in these planes at $t = 55$ and 66: the x-z plane located at $y = 0.3\lambda_z$ (top), the x-y plane parallel to the bottom slope at a height $z = 0.103\lambda_z$, and the y-z plane located at $x = 0.577\lambda_z$ (bottom).

Nokes (1989), who conducted a related experiment in the laboratory over a 30° slope. They describe a turbulent bore that passed through the boundary layer each wave period. For example, note that at $t = 55$ and 66 there are distinct stratified regions between the two bores.

The previous figures have indicated the structure of the flow in only one vertical plane. Next we examine aspects of the three-dimensional nature of the flow during wave breakdown into turbulence. Velocity vectors in three different planes are presented in Fig. 17 at $t = 55$ and 66. The top panels of Fig. 17 show velocity vectors in the same planes as the density fields in Fig. 16. These velocity vectors are plotted on a subset of the grid locations to enhance

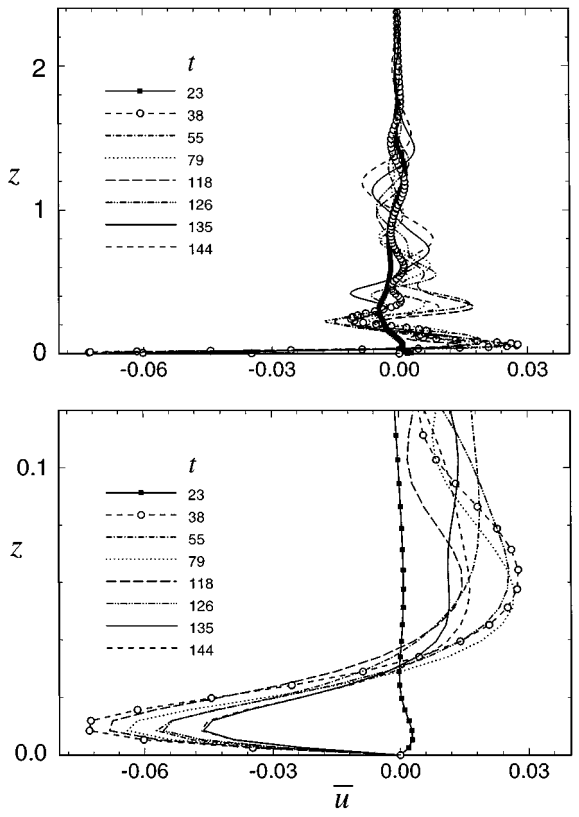

FIG. 18. Mean velocity profiles $\overline{u}(z)$ at different times for the same experiment shown in Figs. 16 and 17 for critically reflecting internal waves with a bottom slope of 30°.

visibility. A reference vector with magnitude $|\mathbf{u}| = 0.12$ is plotted outside the domains to indicate the velocity scales. The flow appears qualitatively similar at the two times shown indicative of the fairly steady turbulent flow. Strong currents converge in the region of the turbulent bore and create a strong region of local mixing and dissipation in the boundary layer. The shear of the oncoming wave is evident in the upper portions of the domain and merges into the bore region as an integral part of the dynamics occurring there. The bore might be termed the "turn around" zone for the internal wave, where the downward moving fluid and upward moving fluid change direction as the plane wave is interrupted by the wall. Between the two turbulent regions a region of downslope flow occurs very near the wall across most of the breadth of the domain (Fig. 18).

In the middle panels of Fig. 17 the velocity components are shown in an x-y plane parallel to the sloping bottom plane at a distance from the wall of $z = 0.103\lambda_z$. The vectors appear to indicate a divergent flow because they show only the components of velocity in the x-y plane and do not include the w component. Several distinct horizontal structures are apparent in the flow. The observed variability in the y-direction is an indication of the importance of the three-dimensionality of the wave breakdown process. If regions of high variability of the v component are compared with the density fields of Fig. 16, then the strongest three-dimensionalities are seen to occur at (and move with) the location of the thermal front. The bottom panels of Fig. 17 show the velocity vectors in a y-z plane located at $x = 0.577\lambda_z$. Here the recirculation in the boundary layer is evident.

The localization of the turbulence appears to be related to the geometry of the problem, particularly the aspect ratio of the horizontal and vertical wavelengths of the oncoming wave, and to the steepness of the bottom slope. Turbulent patches develop initially above the location of the thermal front and have a characteristic thickness of approximately $\lambda_z/3$. After the turbulence is formed it then appears to favor horizontal spreading. The steep slope effectively partitions the boundary layer into regions above and below the turbulent bore and helps to confine the turbulence to a localized region. The fluid in the boundary layer above (ahead) and below (behind) the bore are somewhat insulated from the turbulence by the stratification.

Mean alongslope velocity profiles $\bar{u}(z)$ are plotted as a function of perpendicular distance from the wall in Fig. 18. The top panel shows the domain to a height of $2.4\lambda_z$ while the bottom panel shows only the bottom portion of the domain to a height of $0.12\lambda_z$. At $t = 23$ the oncoming wave train has not yet reached the bottom boundary and the velocity profile reflects the steady laminar boundary currents induced by diffusion of the density field at the wall as predicted by Phillips (1970). At later times, after wave breakdown has commenced the average velocity profiles are similar to one another illustrating the quasi-steady nature of the flow. A consistent feature in the profiles is a thin viscous layer of downslope flow located near the wall at heights $z < 0.025$ which is resolved by approximately ten grid points (at locations of symbols). Three-dimensionality is strongly inhibited in this layer by the presence of the wall due to viscous effects. This feature does not develop for bottom slopes $\alpha < 20^\circ$ and appears to be a mechanism for restratification coupled to the wave breakdown in the bore.

Volume averages of kinetic, potential, and total energies are shown in Fig. 19. The oncoming gravity waves have equipartition of energy (*i.e.*, equal kinetic and potential energy). Also shown in Fig. 19 is the time integrated buoyancy flux $\bar{B}_f$; its negative value indicates a net transfer of potential to kinetic energy. After about $t = 40$ the energy input from the wave forcing mechanism nearly equals the dissipation of energy and the total energy in the system levels off and the system reaches quasi-equilibrium.

Volume integrals of the various terms of the kinetic and total energy equations (3.73) and (3.75) are shown in Fig. 20 as a function of time on an average, per unit volume, basis. After approximately $t = 50$ the energetics of the flow develop in a quasi-steady manner. The bottom panel of Fig. 20 shows the terms in the total energy equation. The dominant

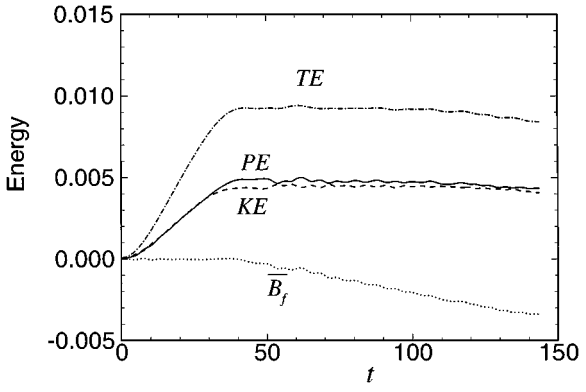

FIG. 19. Volume integrals of kinetic, potential, and total energy and the time integrated buoyancy flux $\bar{B}_f$ for the 30° critical angle experiment.

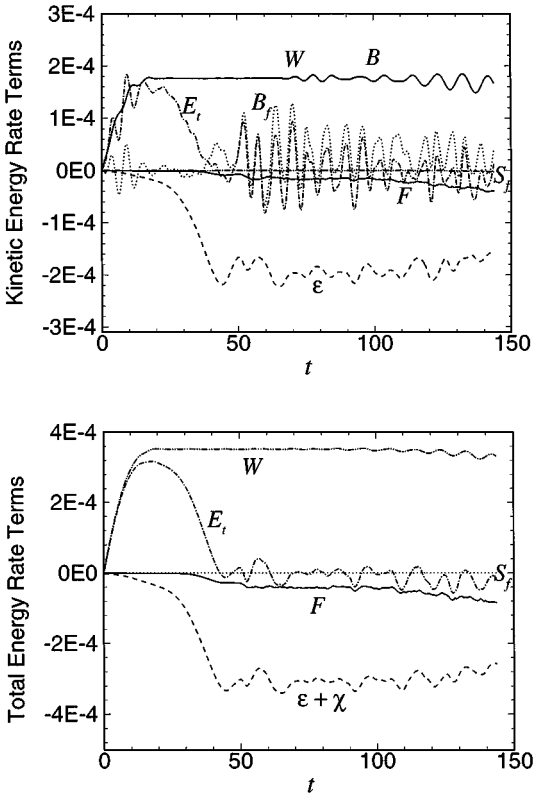

FIG. 20. Volume integrals of terms in the kinetic (top) and (total) energy equation, (3.79) and (3.81): work input (W), rate of change of energy (E_t), dissipation rates (ϵ and χ), filter dissipation (F), buoyancy flux (B_f), flux of energy out of the control volume (S_f), and balance (B).

terms are the work input and loss of energy by turbulent dissipation. The net result is a near constant balance between these major terms.

The terms of the kinetic energy equation show more details of the flow development. A dominant feature is the rapid oscillation of the buoyancy flux. Associated with this is the time rate of change of kinetic energy, which follows the buoyancy flux closely. The oscillations in the buoyancy flux occur at approximately the buoyancy period of 2π. For example, there are 15 maxima and minima in the buoyancy flux between $t = 50$ to $t = 140$, or approximately one per buoyancy period. While not all maxima have the same magnitude, the consistent pattern suggests that oscillations at the buoyancy frequency are a dominant feature of the energetics of the flow.

The work input of kinetic energy achieves a fairly steady value of about 2×10^{-4}. Oscillations in work input begin at about ($t \approx 70$) and may be attributed to the superposition of incoming and outgoing energy, modulating the local velocity field in the forcing region and hence the work input, which is the product of the local velocity and forcing terms (3.71). This does not, however, change the amplitude of the downward directed wave train.

The balance of kinetic energy is very good (B and W are indistinguishable in Fig. 20); typically the errors are less than 1%. This small error may also be attributed to different integration techniques. A simple method of integration was used for the energy rate terms, based upon summation of the grid values for the velocities, weighted by the local volume of

the variable grid. It was found later that the use of a more sophisticated numerical integration method, such as the trapezoidal or Simpson's rule, could also alter some of the integrals by approximately 1%. The general conclusion is that the energy balance is very good, and the individual terms are representative of the energetics in the fluid.

The dissipation rates in Fig. 20 appear as negative quantities, meaning a loss of kinetic or total energy. The loss of kinetic energy by the compact filter subgrid-scale model has been separated from the resolved dissipation. Comparison of these magnitudes shows that most of the dissipation has been resolved. Time integration of the losses of energy shows that, on a $129 \times 65 \times 130$ grid, 92% of the kinetic energy dissipation has occurred through ϵ at well resolved scales and 8% of the kinetic energy dissipation has been accomplished by the subgrid-scale filter.

Figure 21 plots gray scale contours of the dissipation Reynolds number, $Re_d = \epsilon/\nu N^2$, in the same three planes as Fig. 17 at $t = 55$. The main point of the figure is that nearly all of the dissipation occurs in the turbulent boundary layer, in an inhomogeneous fashion. Ivey and Nokes (1989) have used Re_d to predict transition to turbulence. They suggest that for $Re_d = \epsilon/\nu N^2 > 10$ there may be a universal transition point for stratified turbulence. The streaks nearest the wall, seen in the top frame of Fig. 21, have $Re_d > 500$, while the core of the turbulent bore has regions with $Re_d \approx 100$. The bottom two frames of Fig. 21, illustrating a top view and an end view, show the three-dimensional structure of the turbulence. While the average values of the dissipation rate are somewhat uniform in the y-direction, the contours of dissipation rate are comprised of strong streaks indicative of local variability.

The strongest dissipation occurs in the viscous sublayer for $z < 0.01\lambda_z$. Horizontally averaged dissipation rates are plotted as a function of z in Fig. 22. Vertical integration of the dissipation rates indicate that approximately 40% of the total wave energy dissipation occurs in the viscous layer near the wall (39% at well resolved length scales and 1% from the filter) for this flow at $RE = 1000$. At higher Reynolds numbers the contribution to the total dissipation rate from the viscous layer decreases significantly while remaining well resolved, for example, at $Re = 2000$ the contribution to the total dissiption rate from the viscous layer is approximately 20% (19% resolved, 1% filter). The spatial inhomogeneity of the flow makes it difficult to determine the appropriate average dissipation rate for estimating a total Re_d for the turbulent boundary layer. If ϵ is averaged just in the core of the turbulent bore, then $Re_d \approx 30$. If, however, ϵ is spatially averaged across the boundary layer, to a height of $z = \lambda_z/4$ then $Re_d \approx 7$.

Finally, results from releasing a passive "dye" in the near wall region are shown in Fig. 23. The initial concentration, C, at $t = 0$, of the dye near the boundary is $C = 1.0$ for $z < 0.15\lambda_z$, falling off between $0.15\lambda_z < z < 0.3\lambda_z$, and $C = 0$ for $z \geq 0.3\lambda_z$. As mixing occurs in the turbulent layer the concentration of dye near the wall decreases. Contour levels of $0 < C < 0.5$ are plotted in Fig. 23 at $t = 0$, 76, and 144. A horizontal intrusion of dye is observed to steadily work its way into the interior domain, approximately following surfaces of constant density. At $t = 144$ two distinct horizontal dye layers are evident located at $z_T \approx 0.5\lambda_z$ and $z_T \approx 0.8\lambda_z$. Thus by $t = 144$, approximately nine wave periods after mixing begins, the dye is present in a layer approximately twice as thick as when initially released. The important point revealed by the motion of the dye is that there is a slow circulation driven by buoyancy forces as fluid is mixed in the boundary layer. We conclude that the net effects of boundary mixing are not confined to the boundary layer region but are communicated horizontally to the interior stratified fluid.

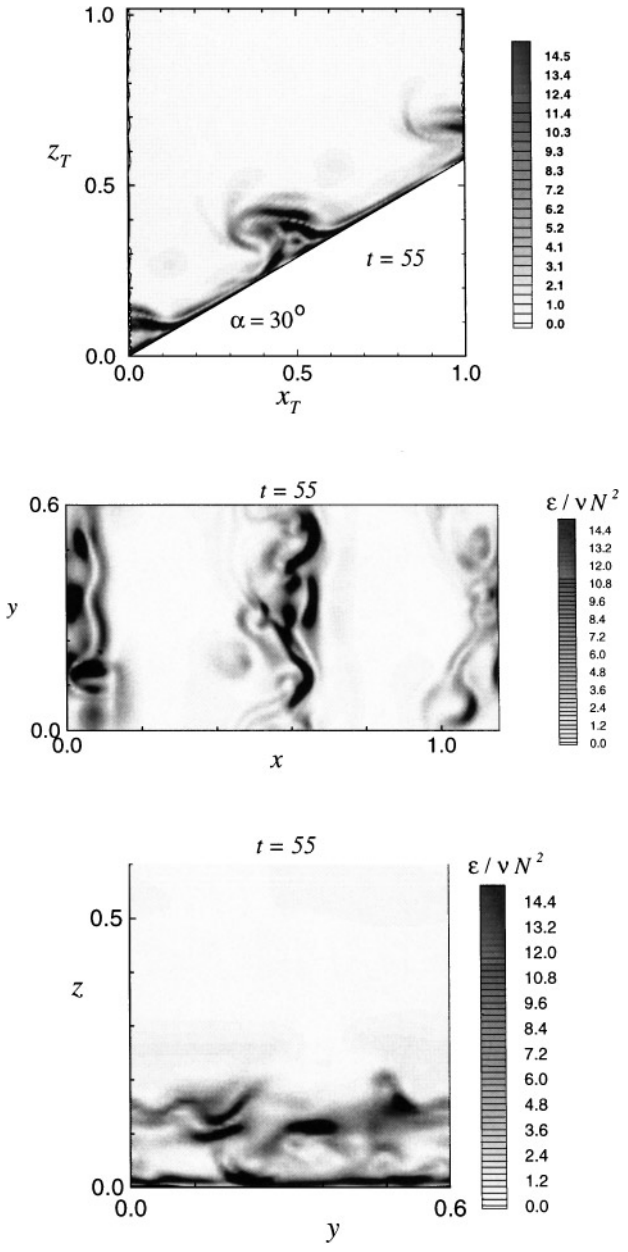

FIG. 21. Kinetic energy dissipation rate normalized by νN^2 in these planes at $t = 55$: the x-z plane located by $y = 0.3\lambda_z$ (top), the x-y plane parallel to the bottom slope at a height $z = 0.103\lambda_z$, and the y-z plane located at $x = 0.577\lambda_z$ (bottom).

Results from the 30° critical angle experiment have provided an example of how the model performs for the internal wave reflection problem at a moderate Reynolds number. We have observed that the oncoming waves transition to turbulence in a boundary layer of approximate thickness $\lambda_z/3$ as it reflects from the bottom wall. The turbulence is localized and moves upslope at the x-component of the phase speed of the oncoming wave. A quasi-steady flow develops in which the oncoming wave energy is dissipated near the wall while mixing the fluid in the boundary layer.

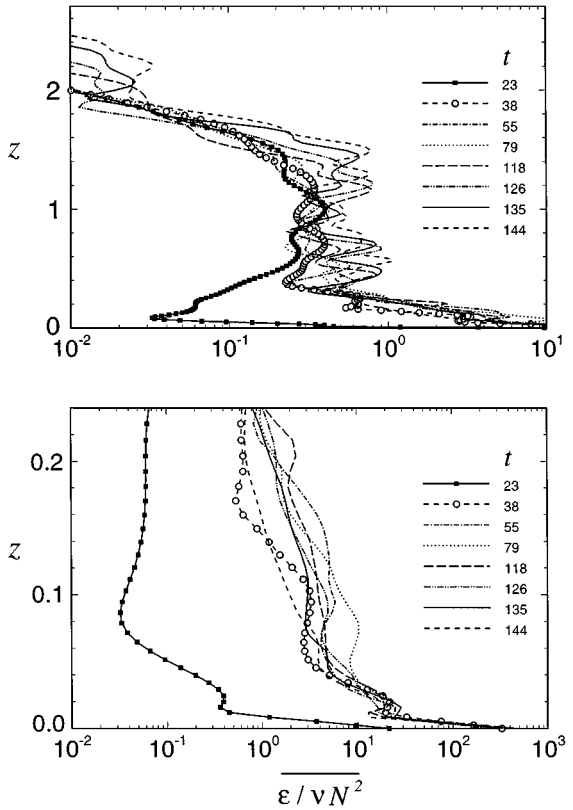

FIG. 22. Average kinetic energy dissipation rate $\overline{\epsilon}(z)$ at different times for the same experiment shown in Figs. 16–21 for critically reflecting internal waves with a bottom slope of 30°.

5. SUMMARY

We have presented a new three-dimensional Navier–Stokes solver for direct numerical and large eddy simulations of a turbulent boundary layer in a stratified fluid subject to the Boussinesq approximation. The model was designed to study the problem of internal wave reflection from sloping boundaries that can result in wave breakdown into a turbulent boundary layer. Internal waves are generated by a new method that forces moderate amplitude monochromatic oncoming waves at specified wavelengths and frequencies. An analytic solutionhas been presented for the wave forcing mechanism that predicts properties of the resulting forced wave. It was found that the vertical extent of the forcing region should be greater than or equal to the vertical wavelength of the desired monochromatic wave train to yield satisfactory results.

The model is periodic in two dimensions and in the third dimension employs a wave absorbing layer at the upper surface and a solid sloping surface at the bottom boundary. The equations of fluid motion are solved in a rotated coordinate system aligned with the sloping bottom topography. Boundary currents that arise in a stratified fluid over slopes (Phillips, 1970) balancing mass diffusion with upslope convection have been included in the model initialization.

The combination of numerical techniques in the model make it generally robust and well suited for application to boundary layer and other wave propagation problems. The

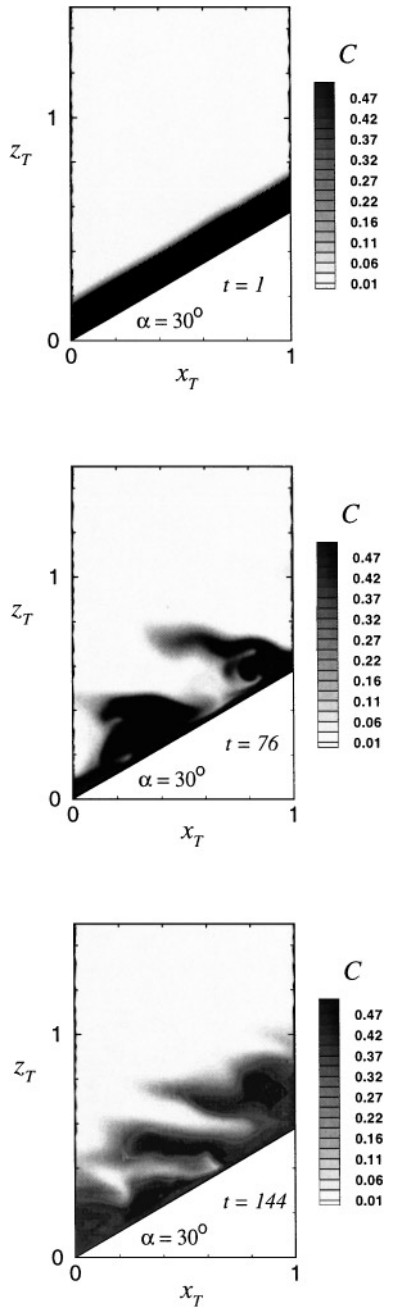

FIG. 23. Dye field concentrations at $t = 1$, 76, and 144.

time discretization scheme is a third-order Adams–Bashforth realization of the projection method. Greater efficiency is introduced by using a variable time-stepping scheme that allows the time step to be adjusted, based upon results from the combined temporal and spatial numerical stability analysis. The spatial discretization in the model uses compact finite differencing techniques (Lele, 1992), which have near spectral accuracy in their ability to resolve a wide range of wavenumbers with minimal phase errors. A variable-mesh grid is

used to cluster computational nodes near the physical boundary at the sea bed. The variable grid is mapped onto a uniform grid in computational space by an algebraic relationship. Calculations on grids of up to $129 \times 129 \times 130$ ($\simeq$2.1 million) points have been conducted, and the model achieves significant efficiencies through vectorization and parallelization. The pressure field is determined to fourth-order accuracy by taking advantage of the periodicities in the problem and by decoupling the directional dependencies of the pressure field in Fourier wave number space to allow gains from both vectorization and direct matrix inversion of the pressure coefficients.

In the gravity wave reflection flow, the main interactions that occur are at large scales and can be well resolved. Numerical experiments have been conducted at Reynolds numbers $500 < Re < 5{,}000$. For the majority of the experiments, at a moderately low Reynolds number (e.g., $Re < 2500$), the model represents a direct numerical simulation of the boundary layer. At a higher Reynolds number attention is focused on the large scales of motions and the manner in which energy is transferred to the intermediate-scale motions; phenomena at smaller, dissipative scales are parameterized. For approximately $Re > 2500$ the model may be considered a large eddy simulation (LES) of the flow, with an additional hyperviscosity filter ($\nabla^4\mathbf{u}$) used to dissipate excess energy from the subgrid scales of motion.

The utility of the model has been examined in a number of simplified test problems as well as for internal wave reflection from sloping topography. Results of numerical simulations have shown good agreement with theory and laboratory studies. New insights into the physics of the gravity wave reflection problem have been revealed through these numerical simulations. The model is generally robust and the combination of numerical techniques it employs make it well suited for application to boundary layer problems.

APPENDIX A: ANALYTIC SOLUTION FOR FORCING

In Subsection 2.4 the forced response for a numerical solution was determined for the equations

$$A_f'''(z) + 4m^2 A_f'(z) = -\frac{A}{\omega k} F'''(z) + \frac{2A(k^2 - m^2)}{\omega k} F'(z) \tag{A1}$$

$$B_f'''(z) + 4m^2 B_f'(z) = \frac{4Am}{\omega k}(k^2 + m^2) F(z) \tag{A2}$$

for $F(z) = \exp[-b(z - z_0)^2]$. Here we present an analytic solution for B_f and A_f when $F(z) = \sin^2(z)$ on the interval $0 \le z \le \pi$. Three boundary conditions on $B_f(z)$ are used: at $z = 0$, $B_f = 0$ and $B_f' = 0$, and at $z = \pi$, $B_f' = 0$. The same boundary conditions are used for $A_f(z)$. The solutions are

$$A_f(z) = \frac{A(2 + k^2 - m^2)}{4\omega k(1 - m^2)}[\cos(2z) - 1], \tag{A3}$$

$$B_f(z) = \frac{4Am}{\omega k}(k^2 + m^2)\left[\frac{-\sin^2(m\pi)}{8m^3 \sin(2m\pi)(1 - m^2)} + \frac{\sin(m\pi)\cos(2mz)}{8m^2 \sin(2m\pi)(1 - m^2)} - \frac{\sin(2mz)}{16m^3(1 - m^2)} + \frac{z}{8m^2} + \frac{\sin(2z)}{16(1 - m^2)}\right]. \tag{A4}$$

A_f, B_f, and F are plotted in Fig. 24 for two different values of A, k, m, and ω. Here the forced wave propagates upward, to increasing values of z.

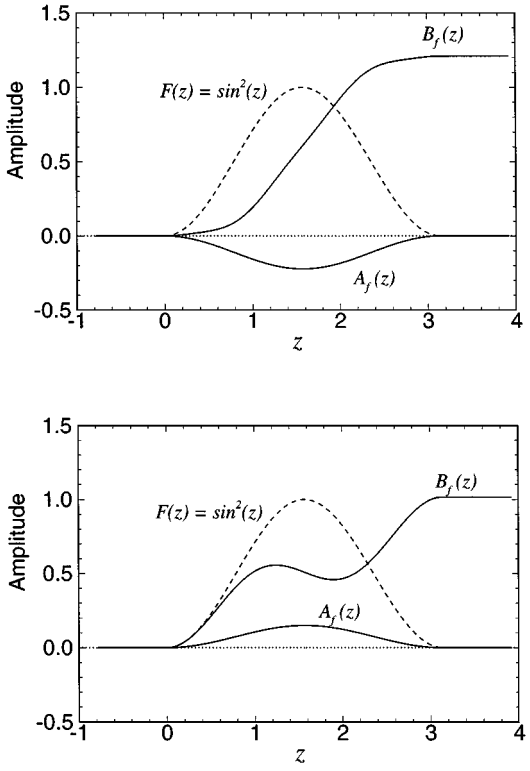

FIG. 24. Shape functions for A_f and B_f, from (A3) and (A4) with parameters $A = 0.15, k = 1.80, m = 3.33, \omega = 0.474$ (top); and $A = 0.08, k = 0.90, m = 1.43, \omega = 0.532$ (top).

The resulting shape function B_f is not sensitive to the ratio $\frac{2\pi}{m}/L_F$ in the same manner as were the results for $F(z) = \exp[-b(z - z_0)^2]$. Here the results are sufficiently smooth outside the forcing region so long as $1-m^2$ does not approach zero at which value the solution contains a singularity. The sensitivity of $B_f(z)$ on $\frac{2\pi}{m}/L_F$ for $F(z) = \exp[-b(z-z_0)^2]$ may be caused by the frequency content of $\exp[-b(z - z_0)^2]$ which contains an infinite series of sine waves each containing singularities at different values of m.

We note, however, that for $F(z) = \sin^2(z)$, the resulting shape of B_f responds differently within the forcing region when either $(1 - m^2)$ or $(2 + k^2 - m^2)$ change sign, which causes A_f to change sign also. For the case when A_f and B_f are of opposite sign (top panel of Fig. 24) the forced waves grow continuously. When A_f and B_f are both positive (bottom panel) B_f decreases in the center of the forcing region.

APPENDIX B: COMPACT FILTERING ON VARIABLE GRID

It was shown in Subsection 3.2 that the filtered field can be obtained on the uniform grid by (3.14)

$$0.4\breve{u}_{i-1} + \breve{u}_i + 0.4\breve{u}_{i+1} = 0.4u_{i-1} + u_i + 0.4u_{i+1} - \frac{1}{80}(u_{i+2} - 4u_{i+1} + 6u_i - 4u_{i-1} + u_{i-2}), \qquad \text{(B1)}$$

which is equivalent to writing

$$0.4\check{u}_{i-1} + \check{u}_i + 0.4\check{u}_{i+1} = 0.4u_{i-1} + u_i + 0.4u_{i+1} - \frac{1}{5}(\Delta x)^4 \left.\frac{\partial^4 u}{\partial x^4}\right|_i . \tag{B2}$$

In the discussion on grid metrics in Subsection 3.5 the equivalent expression for the fourth derivative is given by (3.52)

$$\frac{\partial^4 u}{\partial z^4} = \Gamma_1^4(\zeta)\frac{\partial^4 u}{\partial \zeta^4} + 6\Gamma_1^2(\zeta)\Gamma_2(\zeta)\frac{\partial^3 u}{\partial \zeta^3} + \left[4\Gamma_1(\zeta)\Gamma_3(\zeta) + 3\Gamma_2^2(\zeta)\right]\frac{\partial^2 u}{\partial \zeta^2} + \Gamma_4(\zeta)\frac{\partial u}{\partial \zeta}, \tag{B3}$$

where Γ_1–Γ_4 are given above in Subsection 3.6. Combining Eqs. (B2) and (B3) yields the fourth-order compact filter on the clustered grid

$$\begin{aligned} 0.4\check{u}_{i-1} + \check{u}_i + 0.4\check{u}_{i+1} = {} & 0.4u_{i-1} + u_i + 0.4u_{i+1} \\ & - \frac{1}{80}(u_{i+2} - 4u_{i+1} + 6u_i - 4u_{i-1} + u_{i-2}) \\ & - \frac{\Delta\zeta}{80}\left(\frac{6\Gamma_2}{\Gamma_1^2}\right)_i \left(\frac{u_{i+2} - 2u_{i+1} + 2u_{i-1} - u_{i-2}}{2}\right) \\ & - \frac{\Delta\zeta^2}{80}\left(\frac{4\Gamma_3}{\Gamma_1^3} + \frac{3\Gamma_2^2}{\Gamma_1^4}\right)_i (u_{i+1} - 2u_i + u_{i-1}) \\ & - \frac{\Delta\zeta^3}{80}\left(\frac{\Gamma_4}{\Gamma_1^4}\right)_i \left(\frac{u_{i+1} - u_{i-1}}{2}\right). \end{aligned} \tag{B4}$$

ACKNOWLEDGMENTS

This work was supported primarily under U.S. Navy Office of Naval Research (ONR) Contract N00014-90-J-1112. Support was also provided for D.N.S. as a Post-Doctoral researcher by ONR Contract N00014-95-1-0047 through a grant to J.S. Allen and R.A. Holman at Oregon State University. Supercomputer support was obtained from NCSA-UIUC and by the College of Oceanic and Atmospheric Sciences, OSU through a grant to M.R. Abbott from the NASA-EOS program.

REFERENCES

Adam, Y. (1977). Highly accurate compact implicit methods and boundary conditions, *J. Comput. Phys.* **24**, 10.

Anderson, D. A., Tannehill, J. C., and Pletcher, R. H. (1984). *Computational Fluid Mechanics and Heat Transfer* (Hemisphere, New York).

Bell, J. B., Colella, P., and Glaz, H. M. (1989). A second-order projection method for the incompressible Navier–Stokes equations, *J. Comput. Phys.* **85**, 257.

Bender, C. M., and Orszag, S. A. (1978). *Advanced Mathematical Methods for Scientists and Engineers* (McGraw–Hill, New York).

Cacchione, D., and Wunsch, C. (1974). Experimental study of internal waves over a slope, *J. Fluid Mech.* **66**, 223.

Canuto, C., Hussaini, M. Y., Quarteroni, A., and Zang, T. A. (1988). *Spectral Methods in Fluid Dynamics* (Springer-Verlag, New York).

Chorin, A. J. (1968). Numerical solution of the Navier–Stokes equations, *Math. Comp.* **22**, 745.

Chorin, A. J. (1984). Book review, computational methods for fluid flow, *Bull. Amer. Math. Soc.* **5**, 87.

Davies, H. C. (1976). A lateral boundary formulation for multi-level prediction models, *Quart. J. R. Meteorol. Soc.* **102**, 405.

Davies, H. C. (1983). Limitations of some common lateral boundary schemes used in regional NWP models, *Monthly Weather Rev*. **111**, 1002.

Durran, D. R., and Klemp, J. P. (1983). A compressible model for the simulation of moist mountain waves, *Monthly Weather Rev*. **111**, 2341.

Durran, D. R. (1992). *Computational Fluid Dynamics for Atmospheric Modeling* (Class Notes for ATM 544 and 591, University of Washington).

Durran, D. R. (1991). The third-order Adams–Bashforth method: An attractive alternative to leapfrog time differencing, *Monthly Weather Rev*. **119**(3), 702.

Durran, D. R., Brown, R., Slinn, D. N., and Yang, M. J. (1993). Towards more accurate wave-permeable boundary conditions, *Monthly Weather Rev*. **121**, 604.

Eriksen, C. C. (1998). Internal wave reflection and mixing at Fieberling Guyot, *J. Geophys. Res. Oceans*, in press.

Fletcher, C. A. J. (1991). *Computational Techniques for Fluid Dynamics. Vol. II. Specific Techniques for Different Flow Categories* (Springer-Verlag, New York).

Fortin, M., Peyret, R., and Temam, R. (1971). Calcul des ecoulements d'un fluide visqueux incompressible, in *Lecture Notes in Physics* (Springer-Verlag, New York), Vol. 8, p. 337.

Fovell, R., Durran, D., and Holton, J. R. (1992). Numerical simulations of convectively generated stratospheric gravity waves, *J. Atmospheric Sci*. **49**, 1427.

Garrett, C. (1990). The role of secondary circulation in boundary mixing, *J. Geophys. Res.* **95**(C3), 3181.

Garrett, C. (1991a). Marginal mixing theories, *Atmosphere-Ocean* **29**, 313.

Garrett, C. (1991b). Paradigm lost? in *Dynamics of Oceanic Internal Gravity Waves* (Proceedings, Hawaiian Winter Workshop, University of Hawaii), p. 433.

Gear, C. W., and Watanabe, D. S. (1974). Stability and convergence of variable order multistep methods, *SIAM J. Numer. Anal*. **11**(5), 1044.

Gear, C. W. (1971). *Numerical Initial Value Problems in Ordinary Differential Equations* (Prentice Hall, Englewood Cliffs, NJ).

Gresho, P. M. (1990). On the theory of semi-implicit projection methods for viscous incompressible flow and its implementation via a finite element method that also introduces a nearly consistent mass matrix. Part 1. Theory, *Int. J. Numer. Methods Fluids* **11**, 587.

Gresho, P. M. (1991). Incompressible fluid dynamics: Some fundamental formulation issues, *Ann. Rev. Fluid Mech*. **23**, 413.

Gresho, P. M., and Sani, R. L. (1987). On pressure boundary conditions for the incompressible Navier–Stokes equations, *Int. J. Numer. Methods Fluids* **7**, 1111.

Hirsh, R. S. (1975). Higher order accurate difference solutions of fluid mechanics problems by a compact differencing technique, *J. Comput. Phys.* **19**, 90.

Ivey, G. N., and Nokes, R. I. (1989). Vertical mixing due to the breaking of critical internal waves on sloping boundaries, *J. Fluid Mech.* **204**, 479.

Karniadakis, G. E., Israeli, M., and Orszag, S. A. (1991). High-order splitting methods for the incompressible Navier–Stokes equation, *J. Comput. Phys.* **97**, 414.

Kim, J., and Moin, P. (1985). Application of a fractional-step method to incompressible Navier–Stokes equations, *J. Comput. Phys.* **59**, 308.

Klemp, J. B., and Lilly, D. K. (1978). Numerical simulation of hydrostatic mountain waves, *J. Atmospheric Sci*. **35**, 78.

Kreiss, H. O. (1972). *Math. Comp.* **26**, 605.

Lele, S. K. (1992). Compact finite difference schemes with spectral-like resolution, *J. Comput. Phys.* **103**, 16.

Lesieur, M. (1987). *Turbulence in Fluids: Stochastic and Numerical Modelling* (Nijhoff, Dordrecht).

Maxey, M. R., and Riley, J. J. (1983). Equation of motion for a small rigid sphere in a nonuniform flow, *Phys. Fluids* **26**, 883.

Orszag, S. A., Israeli, M., and Deville, M. O. (1986). Boundary conditions for incompressible flows, *J. Sci. Comput*. **1**(1), 75.

Peyret, R., and Taylor, T. D. (1983). *Computational Methods for Fluid Flow* (Springer-Verlag, New York).

Phillips, O. M. (1977). *The Dynamics of the Upper Ocean* (Cambridge Univ. Press, Cambridge), 2nd ed.

Phillips, O. M. (1970). On flows induced by diffusion in a stably stratified fluid, *Deep-Sea Res.* **17**, 435.

Pond, S., and Pickard, G. L. (1983). *Introductory Dynamical Oceanography* (Permagon, Oxford).

Rai, M. M., and Moin, P. (1991). Direct simulations of turbulent flow using finite-difference schemes, *J. Comput. Phys.* **96**, 15.

Rai, M. M., and Moin, P. (1993). Direct numerical simulation of transition and turbulence in a spatially evolving boundary layer, *J. Comput. Phys.* **109**, 169.

Roberts, J. (1975). *Internal Gravity Waves in the Ocean* (Dekker, New York).

Shih, T. M., Tan, C. H., and Hwang, B. C. (1989). Effects of grid staggering on numerical schemes, *Int. J. Numer. Methods Fluids* **9**, 193.

Slinn, D. N. (1995). *Numerical Simulation of Turbulent Mixing Caused by Internal Wave Reflection from Sloping Boundaries*, Ph.D. Dissertation, University of Washington.

Slinn, D. N., and Riley, J. J. (1998a). Turbulent dynamics of a critically reflecting internal gravity wave, *Theoret. Comput. Fluid Dynam.*, in press.

Slinn, D. N., and Riley, J. J. (1998b). Internal wave reflection from sloping boundaries, to *J. Fluid Mech.*, in press.

Slinn, D. N., and Riley, J. J. (1996). Turbulent mixing in the oceanic boundary layer caused by internal wave reflection from sloping terrain, *Dynam. Atmospheres Oceans* **24,** 51.

Spalart, P. R., Moser. R. D., and Rogers, M. M. (1991). Spectral methods for the Navier–Stokes equations with one infinite and two periodic directions, *J. Comput. Phys.* **96**, 297.

Squires, K. D., and Eaton, J. K. (1990). Particle response and turbulence modification in isotropic turbulence, *Phys. Fluids A* **2**, 1191.

Taylor, J. R. (1993). Turbulence and mixing in the boundary layer generated by shoaling internal waves, *Dynam. Atmospheres Oceans* **19**, 233.

Temam, R. (1969). *Arch. Rational Mech. Anal.* **32**, 377.

Temperton, C. (1983). Self-sorting mixed-radix fast Fourier transforms, *J. Comput. Phys.* **52**, 1.

Thomas, L. H. (1949). *Elliptic Problems in Linear Difference Equations over a Network*, Report, Watson Sci. Comput. Lab., Columbia University, New York.

Thorpe, S. A., and Haines, A. P. (1987). On the reflection of a train of finite-amplitude internal waves from a uniform slope, *J. Fluid Mech.* **178**, 279.

Thorpe, S. A. (1992). Thermal fronts caused by internal gravity waves reflecting from a slope, *J. Phys. Ocean.* **22**, 105–108.

Winters, K. B. (1989). *Intensification and Instability of Internal Gravity Waves at Caustics and Critical Levels*, Ph.D. Thesis, University of Washington.

Winters, K. B., and Riley, J. J. (1992). Instability of internal waves near a critical level, *Dynam. Atmospheres Oceans* **16**, 249.

Winters, K. B., Lombard, P. N., Riley, J. J., and D'Asaro, E. A. (1995). Available potential energy and mixing in density-stratified fluids, *J. Fluid Mech.* **289**, 115.

Wunsch, C. (1970). On oceanic boundary mixing, *Deep-Sea Res.* **17**, 293.